

# JGR Space Physics

## RESEARCH ARTICLE

10.1029/2020JA028275

### Key Points:

- TIDs with partial to nearly fully concentric rings are seen in the GPS TEC over the CONUS with horizontal phase speeds of 150–530 m/s
- The radial dependence of TID periods, horizontal wavelengths and phase speeds are consistent with the GWs being excited by point sources
- Most of the concentric GWs cannot propagate below 100 km; therefore, their source is most likely in the thermosphere

### Correspondence to:

S. L. Vadas,  
[vasha@nwra.com](mailto:vasha@nwra.com)

### Citation:

Vadas, S. L. & Azeem, I. (2021). Concentric secondary gravity waves in the thermosphere and ionosphere over the continental United States on March 25–26, 2015 from deep Convection. *Journal of Geophysical Research: Space Physics*, 126, e2020JA028275. <https://doi.org/10.1029/2020JA028275>

Received 27 MAY 2020

Accepted 27 OCT 2020

## Concentric Secondary Gravity Waves in the Thermosphere and Ionosphere Over the Continental United States on March 25–26, 2015 From Deep Convection

Sharon L. Vadas<sup>1</sup> , and Irfan Azeem<sup>2</sup> 

<sup>1</sup>Northwest Research Associates, Boulder, CO, USA, <sup>2</sup>ASTRA LLC, Louisville, CO, USA

**Abstract** We examine the total electron content (TEC) from GPS receivers over the United States on March 25–26, 2015. We observe partial to nearly fully concentric rings of traveling ionospheric disturbances (TIDs) with centers close to deep convection. Many of these TIDs have observed horizontal phase speeds  $c_H > 300$  m/s, suggesting they are induced by gravity waves (GWs) created in the thermosphere. We investigate the largest-amplitude concentric TIDs at 23:00 UT on March 25 and 01:20 UT on March 26. We find that  $c_H$  and the GW period  $\tau_r$  increase linearly with radius and the horizontal wavelength,  $\lambda_H$ , increases quadratically with radius. This is expected if the GWs are excited by point sources. For these GWs,  $c_H = 150$ –530 m/s,  $\tau_r \sim 8$ –40 min, and  $\lambda_H \sim 100$ –500 km. Using reverse ray-tracing, no GW with  $c_H > 200$  m/s propagates below  $z = 100$  km, 73% of the GWs in the first case cannot propagate below  $z \sim 100$  km, all of the GWs in the second case cannot propagate below  $z \sim 100$  km, and the inferred thermospheric point sources are  $\sim 2$ – $4^\circ$  from deep convection. Because the underlying GWs are most likely excited by a point source and most must be created in the thermosphere, we find that these concentric TIDs are most likely induced by GWs generated in the thermosphere, including those with  $c_H = 150$ –200 m/s. Their close proximity to deep convection and the TEC map asymmetries suggest these TIDs are likely induced by secondary GWs from local horizontal body forces created by the dissipation of primary GWs from deep convection.

## 1. Introduction

Atmospheric gravity waves (GWs) are excited when deep convective plumes push up into the lower stratosphere. Most of these GWs have relatively small phase speeds and large amplitudes, which causes them to break and dissipate in the stratosphere and mesosphere (Alexander et al., 1995; Choi et al., 2007; Chun & Kim, 2008; Holton & Alexander, 1999; Lane et al., 2003). However, a small fraction of the GWs have small amplitudes and large horizontal phase speeds and vertical wavelengths, which allows them to propagate into the thermosphere (Heale et al., 2014; Hickey et al., 2009; Vadas & Fritts, 2004, 2005, 2006; Vadas & Liu, 2009). Here, kinematic viscosity is quite important, because it increases approximately exponentially with altitude (Pitteway & Hines, 1963). This increase creates a situation where GWs with different parameters are eliminated by viscosity at different altitudes (Vadas, 2007, 2013). This so-called “dissipative filtering” acts alongside wind filtering to transform and filter spectra of GWs from below (Fritts & Vadas, 2008). Modeling (Vadas, 2007) and observational (Djuth et al., 1997, 2004; Oliver et al., 1997) studies have shown that the vertical wavelength  $\lambda_z$  of the surviving GWs increases approximately exponentially with altitude up to  $z \sim 220$  km. Above that altitude,  $\lambda_z$  is approximately constant or has a weak dependence with altitude (Nicolls et al., 2014). This may occur because the molecular viscosity  $\mu$  decreases with altitude when the mean free path becomes a substantial fraction of the density scale height  $\mathcal{H}$  (Vadas & Crowley, 2017).

Momentum is deposited when primary GWs dissipate in the thermosphere (Vadas & Fritts, 2004, 2005, 2006; Miyoshi & Fujiwara, 2008; Vadas & Becker, 2019; Yiğit et al., 2009). Specifically for deep convection, this process creates local body forces which accelerate the neutral wind in the direction the primary GWs were propagating, and excites secondary GWs (Vadas et al., 2014; Vadas & Liu, 2009, 2013). These secondary GWs have a wide range of spectral parameters, with horizontal phase speeds  $c_H$  ranging from  $c_H \sim 100$ –600 m/s (Vadas & Crowley, 2010). Secondary GWs can have intrinsic horizontal phase speeds,  $c_{IH}$ , up to 98%

of the sound speed  $c_s$  (Vadas et al., 2019). Thus, for secondary GWs excited in the thermosphere,  $c_{\text{H}}$  can be much greater than  $\sim 300$  m/s because the sound speed is much larger there:

$$c_s = \sqrt{\gamma r \bar{T}}, \quad (1)$$

(e.g., Vadas, 2013), where  $\bar{T}$  is the background temperature,  $r = 8308/X_{\text{MW}} \text{ m}^2 \text{ s}^{-2} \text{ K}^{-1}$ ,  $X_{\text{MW}}$  is the mean molecular weight of the particle in the gas (in g/mol),  $\gamma = C_p/C_v$ , and  $C_p$  and  $C_v$  are the mean specific heats at constant pressure and volume, respectively.  $X_{\text{MW}}$  decreases from 28.9 to 16 and  $\gamma$  increases from 1.4 to 1.67 from the lower atmosphere to the thermosphere (corresponding to the change from diatomic  $\text{N}_2$  and  $\text{O}_2$  to monatomic O). Thus  $c_s$  increases in the thermosphere because  $\bar{T}$  and  $\gamma$  increase and  $X_{\text{MW}}$  decreases. Fast secondary GWs from deep convection with  $c_{\text{H}} > 300$  m/s were seen in modeling studies (Vadas & Liu, 2009, 2013) and in a model/observational study (Vadas & Crowley, 2010). Because such fast GWs usually cannot propagate below the turbopause (Vadas et al., 2019), their sources must be in the thermosphere. Therefore, during geomagnetically quiet times, those GWs in the thermosphere with  $c_{\text{H}} > 300$  m/s are most likely secondary GWs created in the thermosphere.

GWs which propagate in the thermosphere can induce traveling ionospheric disturbances (TIDs) via neutral-ion collisions (Hocke & Schlegel, 1996; Nicolls et al., 2014). Although these TIDs appear to be self-propagating, they are not; indeed, if the underlying GW dissipates, the TID will disappear because of the lack of neutral-ion collisions. Because ions can only move easily along the Earth's magnetic field  $\mathbf{B}$ , only the component of the GW's velocity vector along  $\mathbf{B}$  is relevant to determine its contribution to the amplitude of the induced TID. Therefore, TIDs induced by GWs are not exact tracers of the GWs. However, their presence does indicate the existence of underlying GWs, which can be quite useful for diagnosing GWs and their sources. (Note that the Perkin's Instability creates southwestward-propagating MSTIDs [medium-scale TIDs] in the Northern Hemisphere [Perkins, 1973; Zhou & Mathews, 2006]; these MSTIDs are often seen in the nighttime 630 nm airglow and are not related to GWs [e.g., Martinis et al., 2010]).

Nishioka et al. (2013) discovered concentric TIDs in the GPS TEC over the continental United States (CONUS) which were approximately centered on deep convection associated with a tornado in Moore, Oklahoma on May 20, 2013. The concentric waves were observed for more than 7 h, and were found to have  $\lambda_{\text{H}} \sim 120$  km and  $\tau_{\text{r}} \sim 13$  min, implying  $c_{\text{H}} = \lambda_{\text{H}}/\tau_{\text{r}} = 154$  m/s. The authors concluded "This observational result provides the first clear evidence of a severe meteorological event causing atmospheric waves propagating upward in the upper atmosphere and reaching the ionosphere." Azeem et al. (2015) found partial concentric rings in the total electron content (TEC) associated with a storm in Texas. Crowley et al. (2016) identified TIDs over the CONUS that were associated with the 2011 Tohoku tsunami. Azeem et al. (2017) showed that the characteristics of these latter TIDs reflected the underlying GW characteristics, and used reverse ray tracing to identify their source as being the 2011 Tohoku tsunami off the coast of California. Xu et al. (2019) found partial concentric GWs with  $\lambda_{\text{H}} \sim 200$ –350 km in the stratosphere, mesosphere and ionosphere associated with Hurricane Matthew in October 2016. Chou et al. (2017) observed partial concentric TIDs in the TEC with  $\lambda_{\text{H}} \sim 160$ –200 km,  $\tau_{\text{r}} \sim 8$ –30 min, and  $c_{\text{H}} \sim 106$ –220 m/s from Super Typhoon Meranti on September 13, 2016.

In this study, we examine the properties of partial to nearly fully concentric rings of TIDs in the GPS TEC over the CONUS from 22:00 UT on March 25 to 02:00 UT on March 26, 2015. In Section 2, we briefly review the severe weather conditions reported at that time. We review and derive idealized expressions relating the parameters of GWs excited by a point source with radius in Section 3. In Section 4, we analyze the GWs on March 25, and in Section 5, we analyze the GWs on March 26. We reverse ray trace the observed GWs in Section 6. Section 7 contains our conclusions.

## 2. Severe Weather Over the CONUS on March 25–26, 2015

On March 25, 2015, the National Weather Service reported: "Severe thunderstorms developed late in the afternoon on 25 March 2015 near a warm front that had surged north into northeast Oklahoma and northwest Arkansas. With a highly sheared and unstable air mass in place across the area, discrete supercells

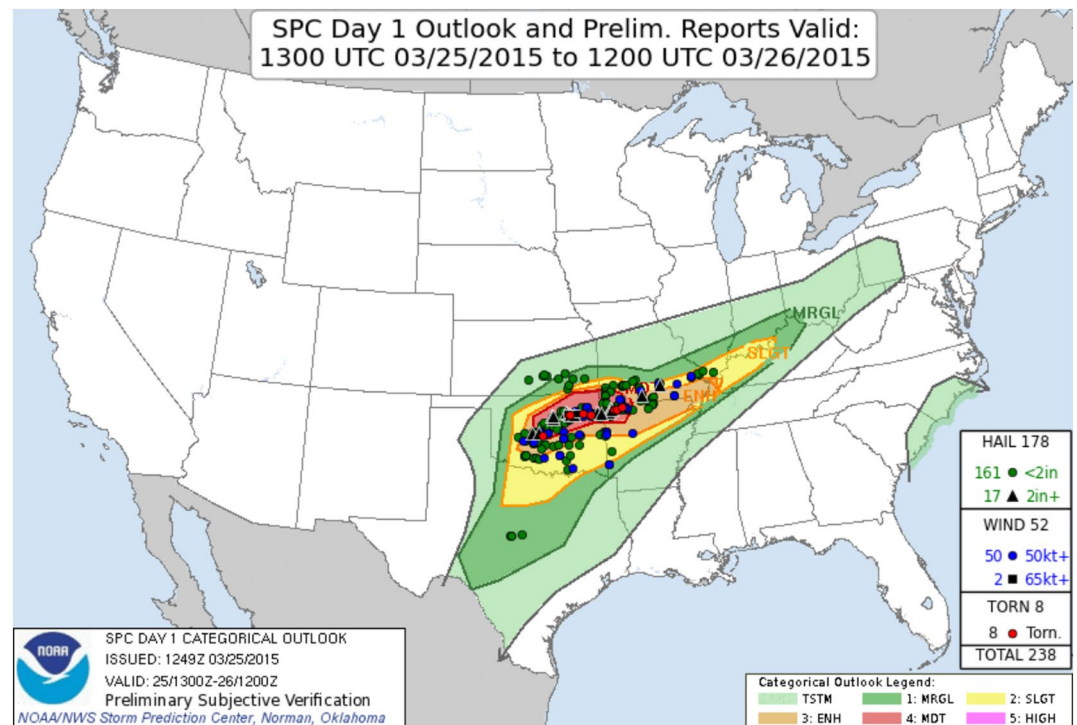


**Figure 1.** NOAA/National Weather Service Storm Prediction Center in Norman, Oklahoma map showing the forecasted weather on 12:49 UT on March 25, 2015 (color contours). The yellow contour indicates where organized severe thunderstorms may occur, the orange contours indicates where a greater concentration of organized severe thunderstorms may occur, while the red contours indicate where widespread severe weather may occur (including tornadoes and severe thunderstorms). The locations where hail, strong winds and tornadoes were reported from 13:00 UT on March 25 to 12:00 UT on March 26 are shown as green dots/black triangles, blue dots/black squares, and red dots, respectively. From [https://www.weather.gov/tsa/weather-event\\_2015mar25](https://www.weather.gov/tsa/weather-event_2015mar25) at the NOAA/Storm Prediction Center.

were able to develop near the warm front late in the afternoon and into the early evening hours. Several tornadoes were spawned from the supercells from west of Tulsa, Oklahoma into northwest Arkansas. As the evening wore on, a cold front surged into the area from the northwest and thunderstorms congealed into a line along the cold front marching to the south and east during the evening and overnight hours. Many of the storms became severe producing large hail and damaging winds before exiting southeast Oklahoma and west-central Arkansas” (from [https://www.weather.gov/tsa/weather-event\\_2015mar25](https://www.weather.gov/tsa/weather-event_2015mar25)). In addition to the severe weather, heavy rains caused flooding across northeast Oklahoma and northwest Arkansas. Figure 1 shows the predicted weather issued by the NOAA/Storm Prediction Center at 12:49 UT on March 25, 2015 (or 07:49 local time [LT]), as well as the resultant reports of tornadoes, hail and strong wind during the following 23 h. During this time, there were 8 reports of tornados, 178 reports of large hail and 52 reports of strong wind. Note that most of the severe weather occurred in Oklahoma, northeastern Arkansas, southern Missouri, and southeast Nebraska.

### 3. Gravity Waves Excited by a Point Source

As we see in the next two sections, the concentric GWs that induce the largest-amplitude concentric TIDs seen during the evening of 25–26 March appear to have been created by point sources. In this section, we review and derive idealized expressions which relate how the parameters of GWs excited by a point source vary with radius in an isothermal atmosphere. Note that some of these expressions have been derived and utilized previously (e.g., Chou et al., 2017; Vadas & Becker, 2019; Vadas et al., 2009).

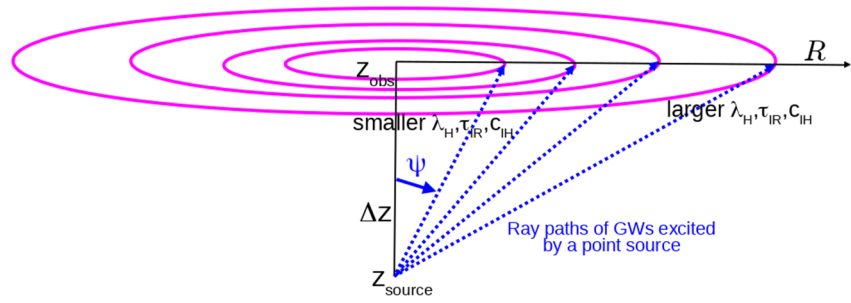


**Figure 2.** Schematic showing the spectrum of GWs created by a point source at  $z_{\text{source}}$  that are observed as concentric rings at  $z_{\text{obs}}$  and  $t_{\text{obs}}$  at the radius  $\mathcal{R}$  (pink rings). Some GW ray paths are shown as dotted blue lines. The angle from the vertical for each GW is  $\psi$ . The GWs at smaller radii have smaller  $\lambda_H$ ,  $\tau_{IR}$ , and  $c_{IH}$ , while those at larger radii have larger  $\lambda_H$ ,  $\tau_{IR}$ , and  $c_{IH}$  from Equations 4, 8, and 13. GW, gravity wave.

We consider the GWs excited by a point source. If sufficiently far away, the GW field resulting from excitation mechanisms such as a deep convective plume, a local horizontal or vertical body force, or a local heating can be approximated as a point source of GWs. Note that local horizontal body forces are created from the dissipation of primary GWs from deep convective plumes (Vadas & Liu, 2009) and orographic forcing (Vadas & Becker, 2018). These point sources tend to excite rich spectra of GWs with widely varying  $\lambda_H$  and  $\lambda_z$  (Vadas & Fritts, 2009; Vadas et al., 2003, 2018). If the effects of winds and dissipation are negligible, concentric rings of GWs are observed at the observation altitude  $z_{\text{obs}}$  (Vadas et al., 2009, 2012; Yue et al., 2009). These rings have cylindrical symmetry for GWs excited by convective plumes, heatings and vertical body forces (Vadas, 2013; Vadas & Fritts, 2009), and are asymmetric along the horizontal axis of the body force direction for a local horizontal body force (Vadas et al., 2003, 2018).

In a windless isothermal background atmosphere, the intrinsic period,  $\tau_{IR}$ , is related to the buoyancy period,  $\tau_B = 2\pi/N_B$ , via

$$\tau_{Ir} = \tau_B / \cos\psi \quad (2)$$

(e.g., Vadas et al., 2009), where  $\psi$  is the angle spanning the GW propagation direction with the zenith and  $N_B$  is the buoyancy frequency. Figure 2 shows a schematic of several ray paths for GWs excited by a point source located at  $z_{\text{source}}$ . Concentric rings of GWs are shown as pink lines at the observation altitude  $z_{\text{obs}}$ . The ray paths for GWs with differing angles  $\psi$  are shown as dotted blue lines. At  $z_{\text{obs}}$ , the radius of each ring is  $\mathcal{R}$ . Since

$$\psi = \tan^{-1}(\mathcal{R} / \Delta z), \quad (3)$$

where  $\Delta z = z_{\text{obs}} - z_{\text{source}}$ , then

$$\tau_{Ir} = \tau_B \left[ \left( \frac{\mathcal{R}}{\Delta z} \right)^2 + 1 \right]^{1/2}. \quad (4)$$

Therefore, for GWs excited by a point source,  $\tau_{Ir}$  increases linearly with  $\mathcal{R}$  when  $\mathcal{R} \gg \Delta z$ .

In an isothermal, windless atmosphere, the GWs that reach  $z_{\text{obs}}$  at the same time  $t_{\text{obs}}$  must have the same vertical group velocity,  $c_{gz}$ , of

$$c_{gz} = \partial \omega_{Ir} / \partial m \sim |\lambda_z| / \tau_{Ir}. \quad (5)$$

Here, we have used the dispersion relation for medium-frequency GWs with  $|\lambda_z| \ll 4\pi\mathcal{H}$  of

$$\omega_{Ir} = \frac{k_H N_B}{|m|} \quad \text{or} \quad \lambda_H \approx |\lambda_z| \tau_{Ir} / \tau_B, \quad (6)$$

where  $k$ ,  $l$  and  $m$  are the zonal, meridional and vertical wavenumbers,  $k_H = \sqrt{k^2 + l^2}$  is the horizontal wavenumber,  $\lambda_H = 2\pi/k_H$ ,  $\lambda_z = 2\pi/m$ ,  $\omega_{Ir} = 2\pi/\tau_{Ir}$ , and  $\mathcal{H}$  is the density scale height. (Note that  $m$  and  $\lambda_z$  are negative for upward-propagating GWs here.) From Equations 4 and 5,

$$|\lambda_z| = |c_{gz}| \tau_{Ir} = |c_{gz}| \tau_B \left[ \left( \frac{\mathcal{R}}{\Delta z} \right)^2 + 1 \right]^{1/2}. \quad (7)$$

Using Equations 4 and 7, Equation 6 becomes

$$\lambda_H \approx |c_{gz}| \tau_B \left[ \left( \frac{\mathcal{R}}{\Delta z} \right)^2 + 1 \right]. \quad (8)$$

Thus, for GWs excited by a point source,  $|\lambda_z|$  increases linearly in  $\mathcal{R}$  and  $\lambda_H$  increases quadratically in  $\mathcal{R}$  when  $\mathcal{R} \gg \Delta z$ . The intrinsic horizontal phase speed,  $c_{IH}$ ,

$$c_{IH} = \omega_{Ir} / k_H = \lambda_H / \tau_{Ir}, \quad (9)$$

also depends on the radius. Here,  $\omega_{Ir} = \omega_r - (k\bar{U} + l\bar{V})$  is the intrinsic frequency,  $\omega_r = 2\pi/\tau_r$  is the observed frequency, and  $\bar{U}$  and  $\bar{V}$  are the zonal and meridional components of the background wind. Since the observed horizontal phase speed is

$$c_H = \omega_r / k_H = \lambda_H / \tau_r, \quad (10)$$

then

$$c_{IH} = c_H - (k\bar{U} + l\bar{V}) / k_H = c_H - U_H, \quad (11)$$

where  $U_H$  is the component of the wind along the GW propagation direction:

$$U_H = \frac{k\bar{U} + l\bar{V}}{k_H} = \bar{U} \cos \theta + \bar{V} \sin \theta. \quad (12)$$

Here,  $k = k_H \cos \theta$ ,  $l = k_H \sin \theta$ , and  $\theta$  is the angle of the GW's propagation direction (counter-clockwise from east) when its path is projected onto the horizontal plane. Using Equations 4 and 8, Equation 9 becomes

$$c_{IH} = |c_{gz}| \left[ \left( \frac{\mathcal{R}}{\Delta z} \right)^2 + 1 \right]^{1/2}. \quad (13)$$

Thus, for GWs excited by a point source in an idealized atmosphere,  $c_{IH}$  increases linearly with radius when  $\mathcal{R} \gg \Delta z$ . Figure 2 summarizes the main features of these results.

## 4. Secondary Gravity Waves on March 25, 2015

### 4.1. GPS TEC Measurements of TIDs

We use over 4,000 dual-frequency GPS receiver sites in the CONUS to “image” the TIDs above this storm system. We combine data from these receivers, which have a 30-s cadence, to produce composite maps of TIDs over the CONUS. We use an elevation mask of 20° to filter out slant TEC measurements at low

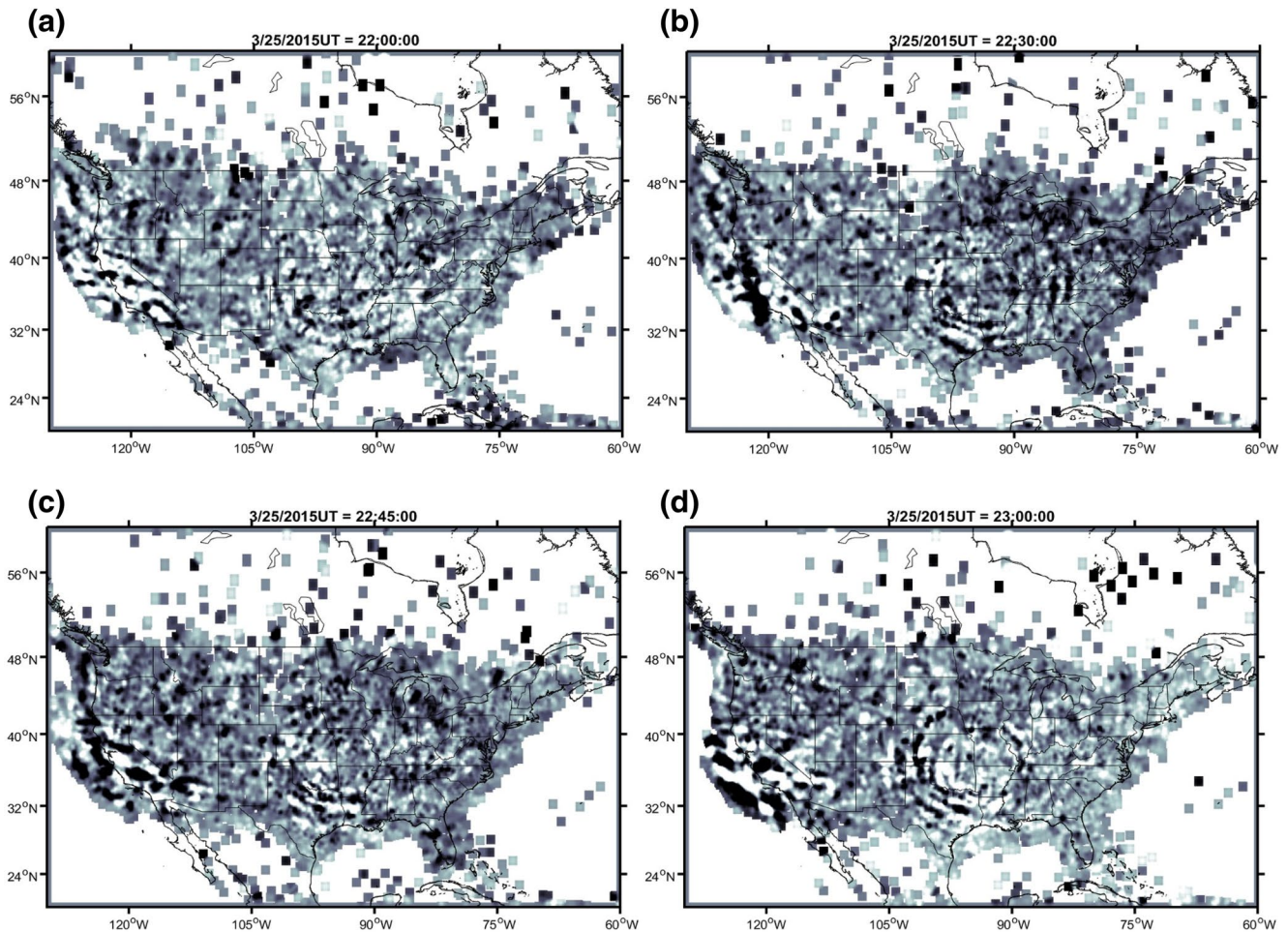


**Figure 3.** GPS TEC maps over the CONUS on March 25, 2015 at (a) 22:00, (b) 22:30, (c) 22:45, and (d) 23:00 UT. CONUS, continental United States.

elevation angles. We calculate TEC perturbations from the TIDs as follows. We use the pseudorange and phase measurements of GPS signals at the L1 (1575.42 MHz) and L2 (1227.6 MHz) frequencies to derive the slant TEC. We convert slant TEC to vertical TEC (VTEC) using the obliquity factor model described by Kaplan and Hagerty (2006) with the assumption that the ionospheric pierce point altitude is 350 km. We then compute perturbations in the TEC by detrending the VTEC using a high-pass filter for each GPS satellite followed by  $0.1^\circ \times 0.1^\circ$  binning in latitude and longitude and horizontal smoothing of the resulting TEC map using a two-dimensional (2D) Gaussian filter with a full width at half maximum of  $0.3^\circ$  in both dimensions. Note that this analysis scheme has been previously employed to study TIDs in the TEC data from distributed GPS receivers (Azeem et al., 2017; Nishioka et al., 2013; Tsugawa et al., 2007). Recently, we added a further processing step to improve the overall image quality of TIDs in the TEC data (Azeem & Barlage, 2017). This image processing step is based on adaptive complex diffusion despeckling filter (Perona & Malik, 1990). The application of the despeckling filter reduces speckle noise and improves the overall image quality, thereby improving the detection threshold and making smaller amplitude TIDs more discernible in the GPS TEC maps.

Figure 3 shows the GPS TEC maps on March 25, 2015 at 22:00, 22:30, 22:45, and 23:00 UT, and Figure 4 shows the maps on March 25 at 23:10, 23:20, 23:30, and 23:40 UT. These maps have  $0.1^\circ \times 0.1^\circ$  resolution. This date occurs during daylight savings time, so the LT in Oklahoma is  $LT = UT - 5$  h. Thus, these maps span 17:00–18:40 LT (5:00–6:40 p.m.) in Oklahoma. Overall, we see many partial and nearly fully concentric rings. The largest-amplitude concentric waves emanate from a region near the intersection of Kansas, Oklahoma, Missouri, and Arkansas. Smaller-amplitude arcs are visible near and south of the Great Lakes

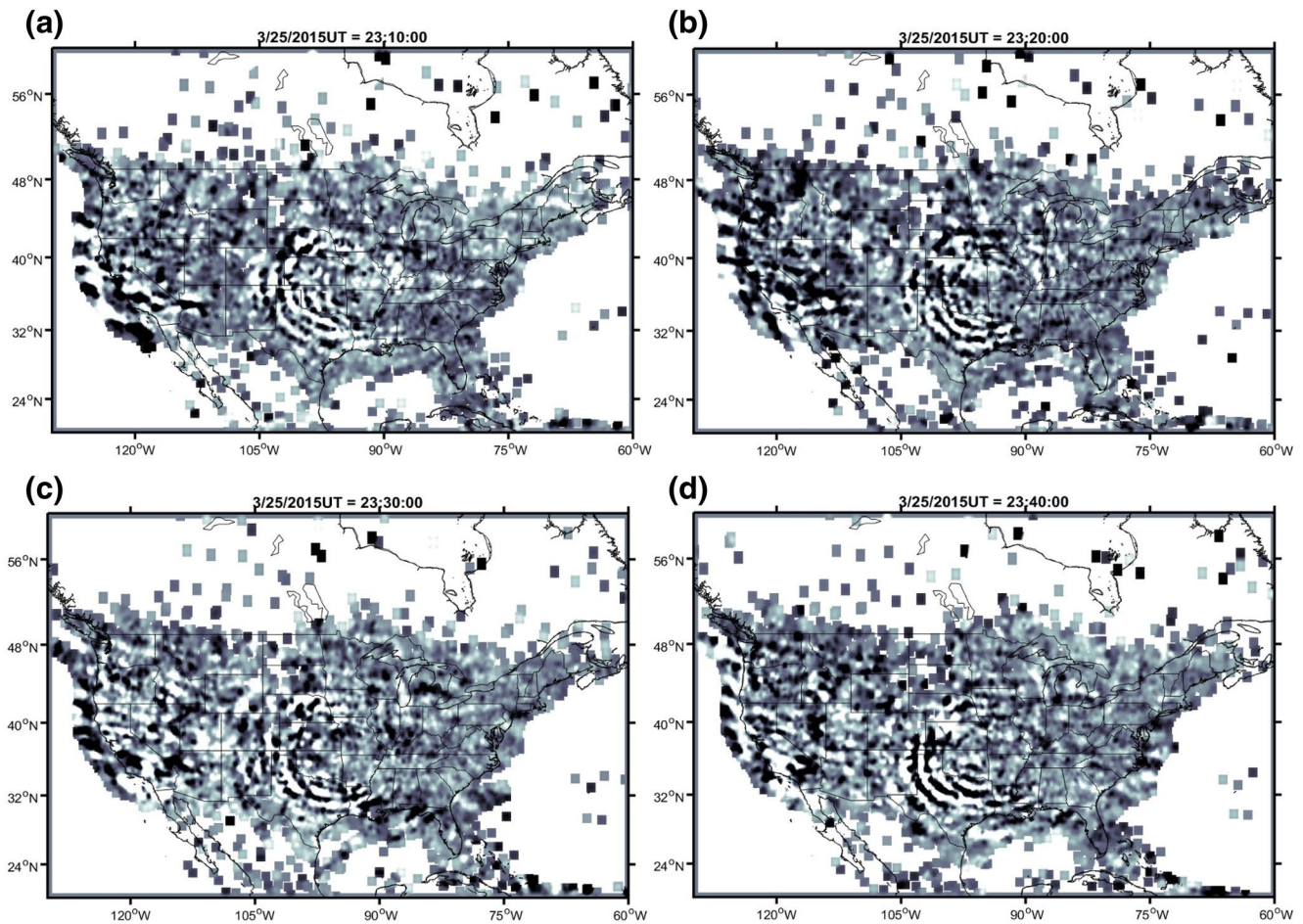


**Figure 4.** GPS TEC maps over the CONUS on March 25, 2015 at (a) 23:10, (b) 23:20, (c) 23:30, and (d) 23:40 UT. CONUS, continental United States.

region, with centers at  $\sim 42^\circ\text{N}$  and  $\sim 88^\circ\text{W}$ . Intersecting wave fronts create constructive and destructive patterns (e.g., over Lake Michigan and Wisconsin at 22:00 UT, and over Minnesota and Wisconsin at 23:00 UT). These TIDs are clearly induced by GWs, because TIDs created by the Perkin's instability only propagate southwestward in the northern hemisphere (e.g., Martinis et al., 2010).

From Figures 3 and 4, the largest-amplitude TIDs propagate westward, southwestward, and southward. We now investigate if this is due to wind and dissipative (from viscosity) filtering. In the middle and upper thermosphere, the horizontal wind is primarily due to the wind component of the in situ diurnal tide from solar EUV heating, which creates a southward wind at 01:00–02:00 LT (just after midnight), a westward wind at 07:00–08:00 LT, a northward wind at 13:00–14:00 LT (just after noon), and an eastward wind at 19:00–20:00 LT (Roble & Ridley, 1994). We construct an atmospheric model using temperatures and density from the empirical NRLMSISE-00 model (Hedin, 1991) and neutral winds from the empirical Horizontal Wind Model (HWM14; Drob et al., 2015). Figure 5a shows the background wind at 23:00 UT (18:00 LT) at  $100^\circ\text{W}$  and  $34^\circ\text{N}$  on March 25. At  $z > 200\text{ km}$ , the wind is approximately eastward, and is northeastward a few hours earlier (not shown). Therefore, the eastward and northeastward GWs will dissipate from viscosity at lower altitudes in the thermosphere than the westward and southwestward GWs because they have smaller  $|\lambda_z|$  and  $c_{\text{TH}}$ , and therefore less dissipative filtering (Fritts & Vadas, 2008). This explains the prevalence of westward, southwestward, and southward-propagating GWs in Figures 3 and 4.

We now estimate the parameters of the largest-amplitude concentric TIDs. As an initial analysis of the TEC maps, we use the Fourier transform to compute the periodicities of the largest-amplitude TIDs within the red box in Figure 6a at 23:12 UT. We find that the GWs which create these TIDs have average values of

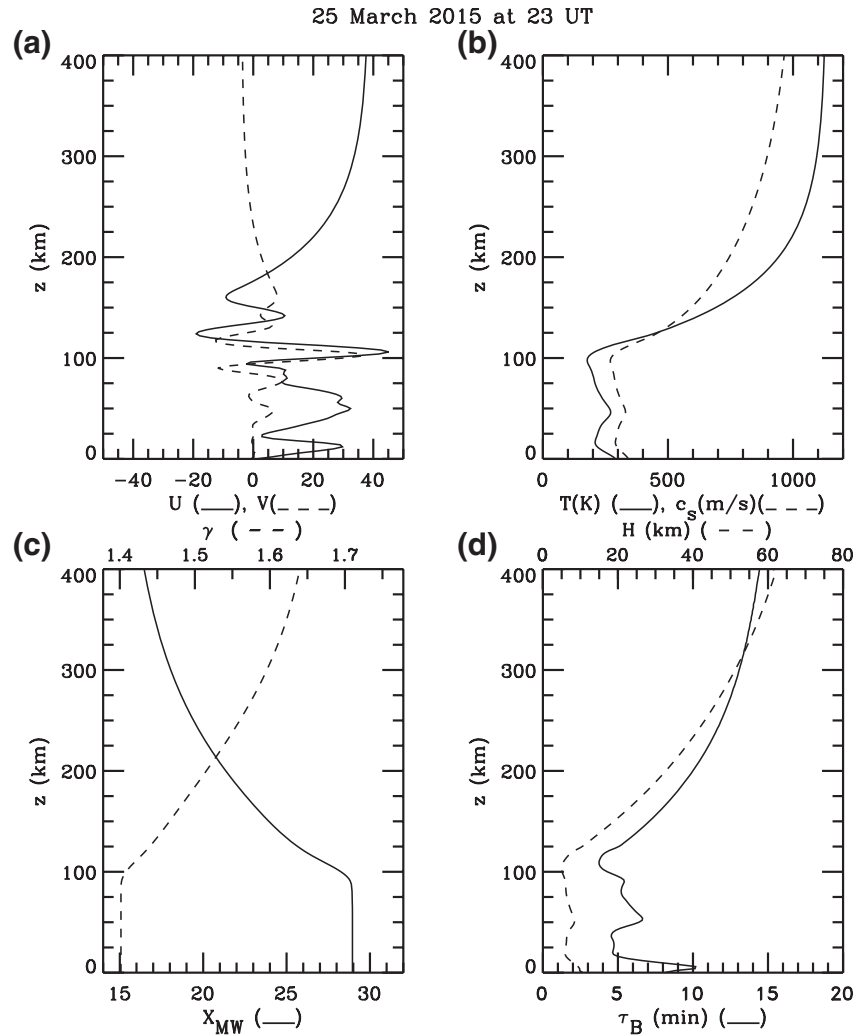


**Figure 5.** Background atmosphere at 23:00 UT on March 25 at 100°W and 34°N. (a)  $\bar{U}$  (solid) and  $\bar{V}$  (dashed). (b)  $\bar{T}$  (solid) and  $c_s$  (dashed). (c)  $X_{MW}$  (solid) and  $\gamma$  (dashed, labels on upper x-axis). (d)  $\tau_B$  (solid) and  $\mathcal{H}$  (dashed, labels on upper x-axis).

$$\begin{aligned}\tau_r &= 22.25 \pm 5.6 \text{ min}, \\ \lambda_H &= 259.66 \pm 8.2 \text{ km}.\end{aligned}\tag{14}$$

We now determine the observed horizontal phase speed,  $c_H$ , using the sequence of TID images from 23:00 to 23:14 UT, and tracking the time it took these southwestward TIDs to pass through the location marked by the “X” in Figure 6a (i.e., at 100°W and 34°N). We find that the GWs which created these TIDs have an average value of

$$c_H = 309.1 \pm 16.3 \text{ m / s}\tag{15}$$

during this time interval. This is consistent with using Equation 10 and the average values of  $\lambda_H$  and  $\tau_r$  from Equation 14. Thus, these GWs have very large values of  $c_H$ , which likely precludes a source location below the turbopause.

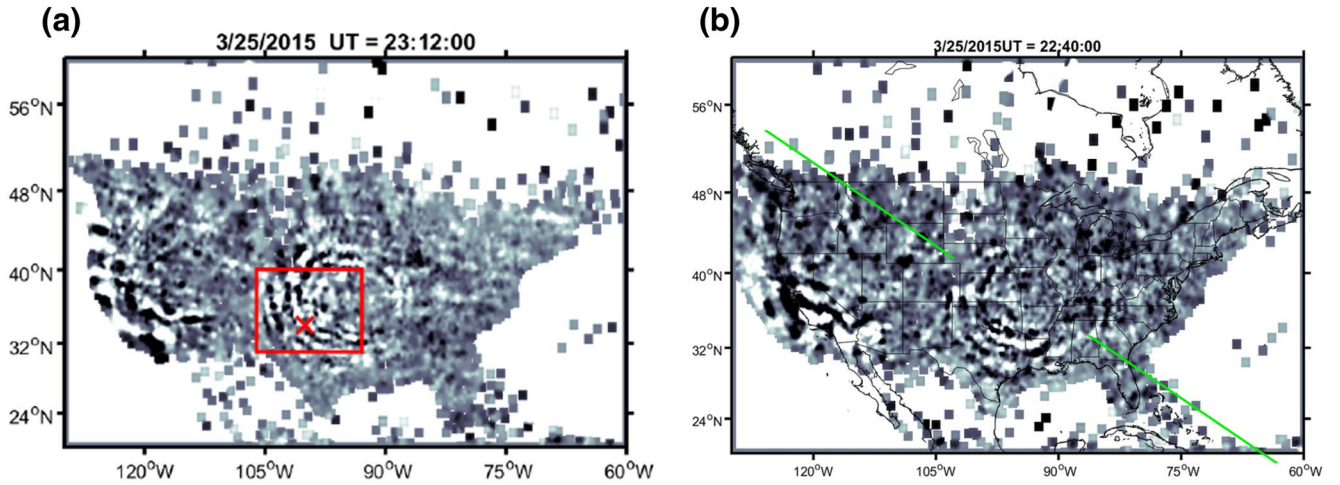


**Figure 6.** (a) GPS TEC map on March 25, 2015 at 23:12 UT. The red box shows the region where the average values of  $\lambda_H$  and  $\tau_r$  are calculated and the “X” shows where  $c_H$  is calculated (see text). (b) GPS TEC map on March 25 at 22:40 UT. Green lines show the line of asymmetry in the concentric rings (see text).

#### 4.2. Comparison of TEC Data With GW Point Source Theory

We now investigate how  $c_H$  depends on the radius  $\mathcal{R}$  from the center of the TEC rings, which we estimate to be at  $36.75^\circ\text{N}$  and  $94.85^\circ\text{W}$ . In Figure 7, we show the TEC perturbations as a function of  $\mathcal{R}$  at 23:15 to 23:22 UT for the angles  $\theta = 180^\circ, 190^\circ,$  and  $208^\circ$  (counter-clockwise from east). Here, we choose a short time interval when the concentric TIDs have relatively large amplitudes and appear clearly in the TEC maps. We overlay the radial locations of the largest-amplitude TIDs as functions of time via dashed, slanted lines. Such an approach has been used in previous studies (Nicolls et al., 2010; Vadas & Becker, 2019; Vadas & Nicolls, 2009). Note that there are also smaller-amplitude TIDs in Figure 7 which we do not analyze here. Figure 8 shows the values of  $c_H$  deduced from the slope of these dashed lines as a function of  $\mathcal{R}$ . Importantly,  $c_H$  increases approximately linearly with  $\mathcal{R}$ , and ranges from  $c_H \simeq 150\text{--}370$  m/s for  $\mathcal{R} = 400$  to  $800$  km. Assuming that  $\bar{U}$  and  $\bar{V}$  do not change very much over these values of  $\theta$  and  $\mathcal{R}$  from the location of the point source, we infer that  $c_{IH}$  also increases approximately linearly with  $\mathcal{R}$ . Using Equation 13, we conclude that the GWs in Figure 8 most likely originate from the same point source.

#### 4.3. Possible Source Altitudes for the Concentric GWs

Since the sound speed near the turbopause is  $c_s \sim 300$  m/s (see Figures 5b), Figure 8 shows that many of the GWs in the spectrum which create the concentric rings have  $c_H$  greater than the value of  $c_s$  near the turbopause. Vadas and Crowley (2010) showed that a GW cannot propagate in an atmosphere if  $c_{IH} \geq c_s$ . This makes sense because an internal GW propagates via molecular interactions, and therefore should not be able to propagate faster than the sound speed. Vadas et al. (2019) further showed that the maximum value of  $c_{IH}$  that a GW can have (denoted  $\max(c_{IH})$ ) is

$$\max(c_{IH}) = \frac{2\sqrt{\gamma-1}}{\gamma} c_s. \quad (16)$$

This maximum value occurs for GWs with  $\lambda_H \gg 4\pi\mathcal{H}$  and  $|\lambda_z| \gg 4\pi\mathcal{H}$ . Below the turbopause,  $\gamma = 1.4$  so that  $\max(c_{IH}) = 0.9c_s$ . At  $z > 200$  km,  $\gamma = 1.667$  so that  $\max(c_{IH}) = 0.98c_s$ . Equation 16 provides a simple way to estimate regions in the atmosphere where a GW cannot propagate without having to perform ray tracing.

From Figure 5b, the minimum sound speed below the turbopause is near the mesopause:  $c_s \sim 270$  m/s at  $z \simeq 98$  km. Using Equation 16, a GW can propagate (upward or downward) through this region only if  $c_{IH} \leq 0.9c_s = 243$  m/s. Because  $\bar{U} \sim 10$  m/s there from Figure 5a, we infer that westward GWs must therefore have  $c_H \leq 233$  m/s to propagate through this region.

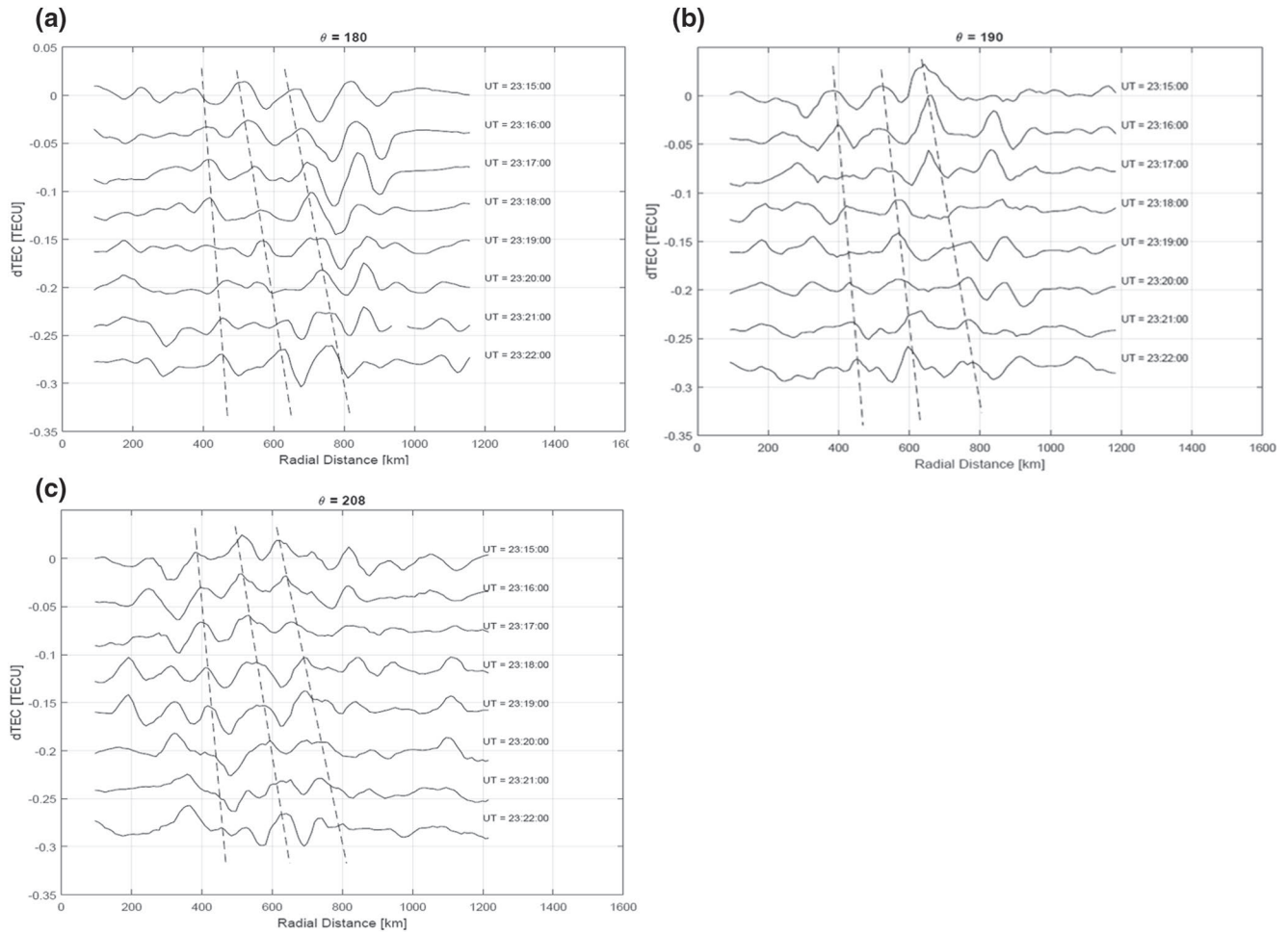


**Figure 7.** The TEC perturbation,  $dTEC$ , (in TECU) as a function of the radial distance  $\mathcal{R}$  from the estimated ring center at  $36.75^\circ\text{N}$  and  $94.85^\circ\text{W}$ . The results are shown every minute from 23:15 to 23:22 UT on March 25, 2015, and are offset by 0.04 TECU from top to bottom (solid curves). Dashed, slanted lines trace the outward motion of the phase lines of the largest-amplitude concentric TIDs in time. (a)  $\theta = 180^\circ$ , (b)  $\theta = 190^\circ$ , (c)  $\theta = 208^\circ$ . TEC, total electron content; TID, traveling ionospheric disturbance.

Figures 9a and 9b show  $c_{IH} / \left[ \frac{2\sqrt{\gamma-1}}{\gamma} c_s \right]$  as functions of  $c_H$  and  $z$  for GWs with propagation angles of  $\theta = 180^\circ$  and  $208^\circ$ , respectively, at 23:00 UT on March 25. Here,  $c_{IH} / \left[ \frac{2\sqrt{\gamma-1}}{\gamma} c_s \right]$  is determined from Equations 11 and 12 using the background atmosphere from Figure 5. From Equation 16, a GW cannot propagate (without tunnelling) for

$$\frac{\gamma c_{IH}}{2\sqrt{\gamma-1}c_s} \geq 1. \quad (17)$$

This is shown via the hatched regions in Figure 9. In addition, GWs may not be able to propagate for values less than one, depending on  $\lambda_H$  and  $\lambda_z$ . We see that GWs with  $c_H > 250\text{--}270$  m/s cannot propagate below the turbopause, and that GWs with  $c_H \sim 220\text{--}250$  m/s cannot propagate through the altitude range  $z \sim 90\text{--}110$  km without reflecting or tunneling. Therefore, the GWs in Figure 8 with  $c_H > 250\text{--}270$  m/s must originate in the thermosphere; therefore, these are not primary GWs from deep convection.

In summary, (1) because  $c_H$  increases linearly with radius in Figure 8, all of these GWs (i.e., with  $c_H = 150 - 370$  m/s) most likely originate from the same point source; and (2) the GWs in Figure 8 with

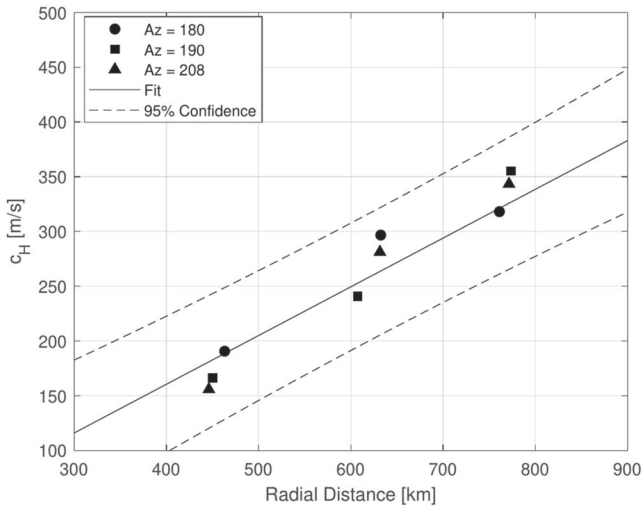


**Figure 8.** The horizontal phase speed,  $c_H$ , of the concentric TIDs as a function of  $\mathcal{R}$  from the estimated center of  $36.75^\circ\text{N}$  and  $94.85^\circ\text{W}$ . Here,  $c_H$  is deduced from the dashed lines in Figure 7. Filled circles, squares, and triangles show the results for  $\theta = 180^\circ$ ,  $190^\circ$ , and  $208^\circ$ , respectively. The solid line shows the best fit to these data points. Dashed lines show 95% confidence intervals. TID, traveling ionospheric disturbance.

$c_H > 250\text{--}270$  m/s cannot propagate below  $z \sim 110$  km. Together, these results imply that all of the GWs in Figure 8, even those with relatively smaller phase speeds of  $c_H \simeq 150\text{--}270$  m/s, are most likely created in the thermosphere. This is important, because it is generally assumed that GWs in the F region with  $c_H < 250$  m/s originate from the lower atmosphere (e.g., Hocke & Schlegel, 1996).

#### 4.4. Spectrograms of the Concentric TIDs

We now examine the parameters of the concentric TIDs closely and more robustly. To estimate the periodicities in a wave packet that is fundamentally nonstationary (time-varying and spatially evolving), we apply discrete wavelet analysis to GPS TEC data and obtain frequency and wavelength spectra at all-time steps for all latitude and longitude grid points of the maps. The utilization of the wavelet spectrogram for GPS TEC data represents a robust method for estimating the periods and horizontal wavelengths of GW packet components. This wavelet spectrogram method was used by Azeem et al. (2017) to estimate the periods and horizontal wavelengths of GW packet components.

We now calculate the spectrogram of the wave periods for the TIDs observed on March 25 at 23:20 UT. 2D TEC perturbations (or TID maps) are computed at each 30 s time step. To compute the TID wave period spectrogram, we take the cross-section of concentric rings at the fixed latitude of

$36.75^\circ\text{N}$  and apply the wavelet transform on the detrended TEC time series at each longitude grid point between  $70^\circ\text{W}$  and  $120^\circ\text{W}$ . Once the wavelet-based time-frequency analysis is completed for all longitude grid points, we compute the normalized wavelet amplitude at 23:20 UT, which corresponds to a time when clear concentric rings were observed in the detrended TEC maps. Figure 10a shows the normalized amplitude of the TID wave period spectrum as a function of longitude. Since  $36.75^\circ\text{N}$  is the latitude of the estimated ring center, these concentric GWs propagate zonally. The periods of the westward-propagating concentric TIDs are seen to increase approximately linearly with radius, with  $\tau_r \sim 8\text{--}35$  min. The linear dependence of  $\tau_r$  with  $\mathcal{R}$  is consistent with GWs excited by a point source (assuming an approximately constant background

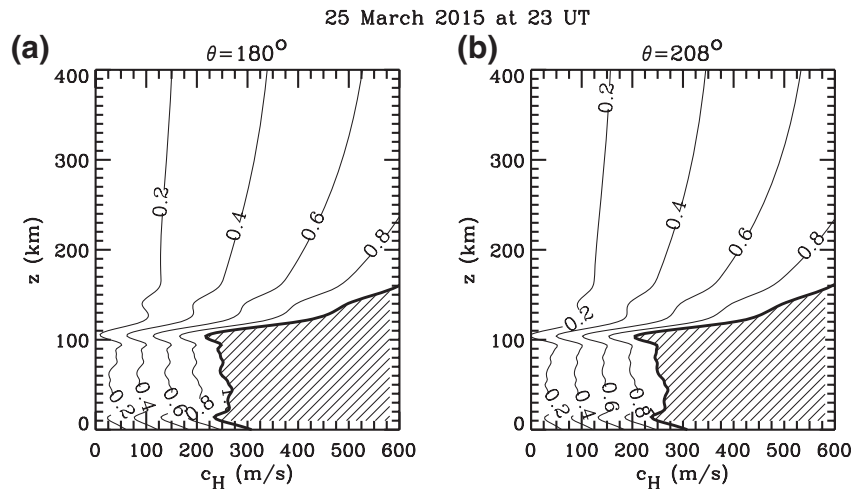


**Figure 9.**  $c_H / \left[ \frac{2\sqrt{\gamma-1}}{\gamma} c_s \right]$  as a function of  $c_H$  and  $z$  at 23:00 UT on March 25 at  $100^\circ\text{W}$  and  $34^\circ\text{N}$ . (a)  $\theta = 180^\circ$ . (b)  $\theta = 208^\circ$ . The value “1” is the thick solid line. The hatched regions show where  $c_H / \left[ \frac{2\sqrt{\gamma-1}}{\gamma} c_s \right] \geq 1$ .

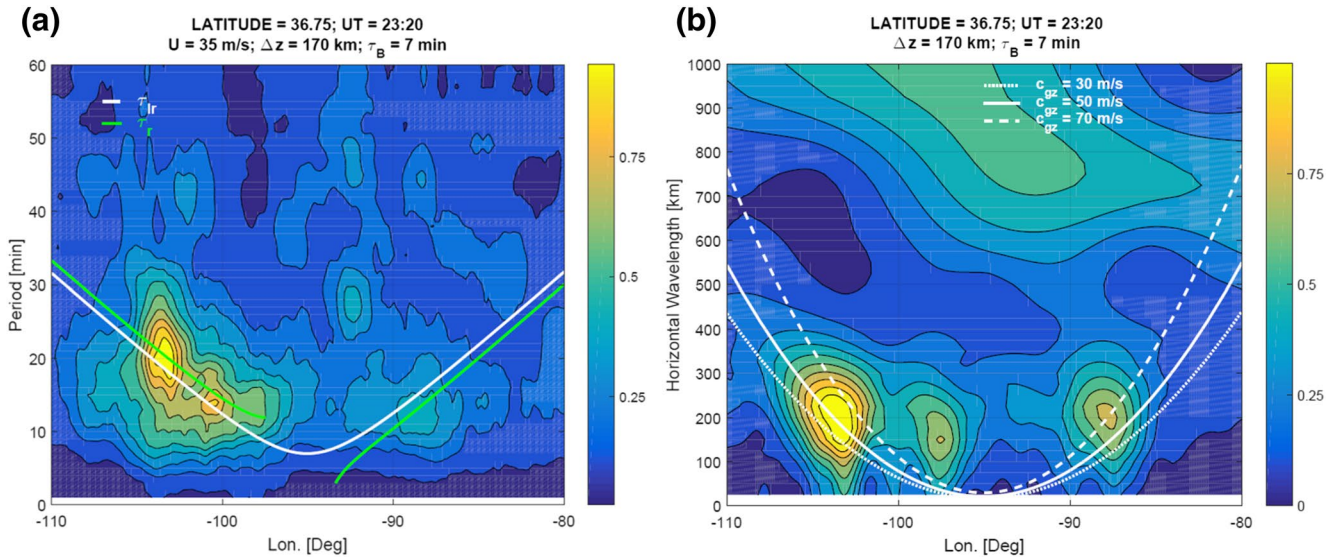


**Figure 10.** Spectrograms of the TIDs at 23:20 UT on March 25 at 36.75°N. (a) Spectrogram as a function of period and longitude (colors). The green and white lines show the observed and intrinsic periods, respectively, for GWs excited by a point source assuming  $\bar{U} = 35 \text{ m/s}$ ,  $\Delta z = 170 \text{ km}$ , and  $\tau_B = 7 \text{ min}$  (see text). (b) Spectrogram as a function of the horizontal wavelength and longitude (colors). The dot, solid and dash white lines show  $c_{gz} = 30, 50, \text{ and } 70 \text{ m/s}$ , respectively, for GWs excited by a point source in an idealized atmosphere using Equation 8 and assuming  $\Delta z = 170 \text{ km}$  and  $\tau_B = 7 \text{ min}$  (see text). GW, gravity wave; TID, traveling ionospheric disturbance.

wind), since  $\tau_{ir}$  increases linearly with  $\mathcal{R}$  for  $\mathcal{R} \gg \Delta z$  (see Equation 4). We now take the background wind into account.

Figure 11 shows the electron density from the International Reference Ionosphere model at 23:00 UT on March 25 at 100°W and 34°N. The F-layer spans  $z \sim 190\text{--}500 \text{ km}$ , with a peak at  $z \sim 270\text{--}280 \text{ km}$ . From Figure 5a,  $\bar{U} \sim 35 \text{ m/s}$  at this peak altitude. For westward-propagating GWs there,  $U_H = -35 \text{ m/s}$ . Here, the minus sign indicates that the wind is opposite to the GW propagation direction. In Figure 10a, we overplot  $\tau_{ir}$  for a point source located in an isothermal, windless background at 36.75°N and 94.85°W using Equation 4 (white lines). Here, we choose  $\Delta z = 170 \text{ km}$  and an average  $\tau_B = 7 \text{ min}$  (see below). To determine  $\tau_r$ , we combine Equations 9–11:

$$\tau_r = \tau_{ir} \left( 1 - \frac{U_H}{c_H} \right). \quad (18)$$

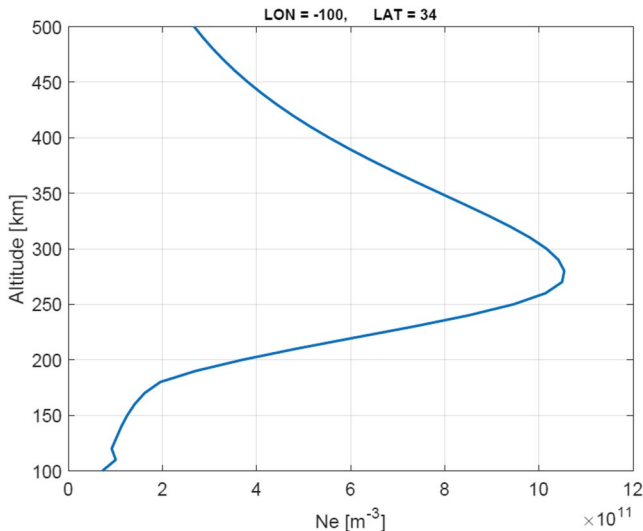


**Figure 11.** Electron density from the IRI model at 23:00 UT on March 25, 2015 and at 100°W and 34°N. IRI, International Reference Ionosphere.

We estimate Equation 18 using the best-fit line for  $c_H$  (as a function of  $\mathcal{R}$ ) from Figure 8. The green line in Figure 10a shows the estimated  $\tau_r$ . Here, we choose  $\Delta z = 170 \text{ km}$  and  $\tau_B = 7 \text{ min}$  in order that the green line agrees reasonably well with the peak of the spectrogram. Note that the curves for  $\tau_r$  and  $\tau_{ir}$  are not best-fit curves, but are intended to illustrate the consistency between the data and idealized point source theory.

Our approach for computing the TID horizontal wavelength spectrum is similar to that for the wave period. We take the cross-section of concentric rings at the fixed latitude of 36.75°N and apply the wavelet transform on the detrended TEC variations along the longitude at each time step. Each wavelet transform at a fixed UT then yields the spectrum of the horizontal wavelength as a function of longitude. Once the wavelet analysis is complete for all UT time steps, we compute the normalized wavelet amplitude at 23:20 UT. Figure 10b shows the spectrogram as a function of longitude at 36.75°N. The peak of the spectrogram increases rapidly with  $\mathcal{R}$  for the westward-propagating TIDs, consistent with the

quadratic dependence of  $\lambda_H$  with  $\mathcal{R}$  for GWs excited by a point source (see Equation 8). These TIDs have  $\lambda_H \sim 50\text{--}400$  km. Note that the peak wave values in Figure 10 are consistent with those from Super Typhoon Meranti (Chou et al., 2017), although the horizontal phase speeds are much larger here (see Figure 8).

We overplot lines of constant vertical group velocity,  $c_{gz}$ , in Figure 10b from Equation 8 in order to provide a consistency check between idealized point source theory with the data, and to allow for a rough estimate of the source height and vertical group velocity. These curves are not fits to the data, and do not take into account Doppler shifting due to background winds. (Note that the distinct smaller-amplitude peak at  $98^\circ\text{W}$  may contain GWs from a different source. These GWs are located at  $\mathcal{R} \sim 300$  km, and are therefore not taken into account in our  $c_H$  analysis shown in Figures 7 and 8.) Reasonable agreement occurs for  $c_{gz} = 50$  m/s. We roughly estimate an approximate propagation time for GWs created by a thermospheric source to perturb the TEC to be

$$\Delta t \sim \frac{\Delta z}{c_{gz}}. \quad (19)$$

For these GWs,  $\Delta t \sim 1$  h. We note that thermospheric body forces from strong deep convection can occur at  $z_{bf} \sim 140$  km (Vadas & Crowley, 2010). Thus, we roughly estimate that the GWs which perturb the TEC are located at  $z \sim z_{bf} + \Delta z \sim 310$  km. This is close to the peak in the F-region shown in Figure 11. (Note that this altitude does not need to agree with the F peak altitude, since these GWs may dissipate from molecular viscosity at higher altitudes than the F peak).

Because of the proximity of the centers of the TID rings to deep convection (see next paragraph and Figure 12), it is quite likely that the thermospheric source which created the underlying GWs are local horizontal body forces created by the dissipation of primary GWs from deep convection. Primary GWs from deep convection take about 1.0–1.5 h to propagate to the thermosphere and create a body force there (Vadas & Liu, 2009, 2013). Adding this to an estimated  $\Delta t \sim 1$  h for the secondary GWs to propagate from their source to perturbing the TEC, we estimate that the deep convective plumes that created these concentric TIDs via secondary (or possibly primary) GWs likely overshoot the tropopause at 20.75–21.25 UT.

Figure 12a shows the cloud top (brightness) temperatures at 21:00 UT on March 25 over the CONUS. The coldest pixels indicate those locations where deep convective plumes overshoot the tropopause and excited high-frequency primary GWs. Deep convection occurred over Missouri, Illinois, Oklahoma, Arkansas, and southern Texas. Figures 12b–12d show the cloud top temperatures every 30 min from 20:00 to 21:30 UT. During this time, the strongest deep convection shifted from a single area in Missouri to several areas near the intersection of Missouri, Oklahoma, and Arkansas. This implies that there were often multiple primary GW sources occurring simultaneously. At 20.83–21.33 UT, there are deep convective plumes within a few hundred kilometers from the center of the concentric TID rings (i.e., at  $36.75^\circ\text{N}$  and  $94.85^\circ\text{W}$ ). This center is mainly southwest of the strongest deep convection. This close proximity may seem surprising, since most of these concentric TIDs appear to be secondary GWs. However, most of the primary GWs from deep convection that create thermospheric body forces have periods of 10–15 min (Vadas & Liu, 2013). From Equation 2, these GWs propagate quite close to the zenith, and move horizontally the distance

$$\Delta L = (z_{bf} - z_{trop}) \frac{\tau_{Ir}}{\tau_B} \quad (20)$$

as they propagate from the tropopause at  $z_{trop}$  to the body force at  $z_{bf}$ . Here, we use  $\cos\psi = \Delta z / \sqrt{\Delta L^2 + \Delta z^2} \approx \Delta z / \Delta L$  for  $\Delta L \gg \Delta z$ , where  $\Delta z = z_{bf} - z_{trop}$  here. For GWs with  $\tau_{Ir} \approx 10\text{--}15$  min,  $\tau_{Ir}/\tau_B \approx 2\text{--}3$ . Setting  $z_{bf} \sim 140$  km and assuming  $z_{trop} \approx 10$  km, we obtain

$$\Delta L \approx 260 - 390 \text{ km} \approx 2 - 4^\circ \quad (21)$$

for these GWs. This agrees well with our estimate of the center of the concentric rings in the TEC maps. Thus, we suggest that southwestward primary GWs from deep convection propagated into the thermosphere and dissipated there, thereby creating southwestward body forces which generated most of the concentric TIDs seen in Figures 3–4 (after thermospheric wind filtering). This would also explain the asymmetry seen in these figures (see next section).

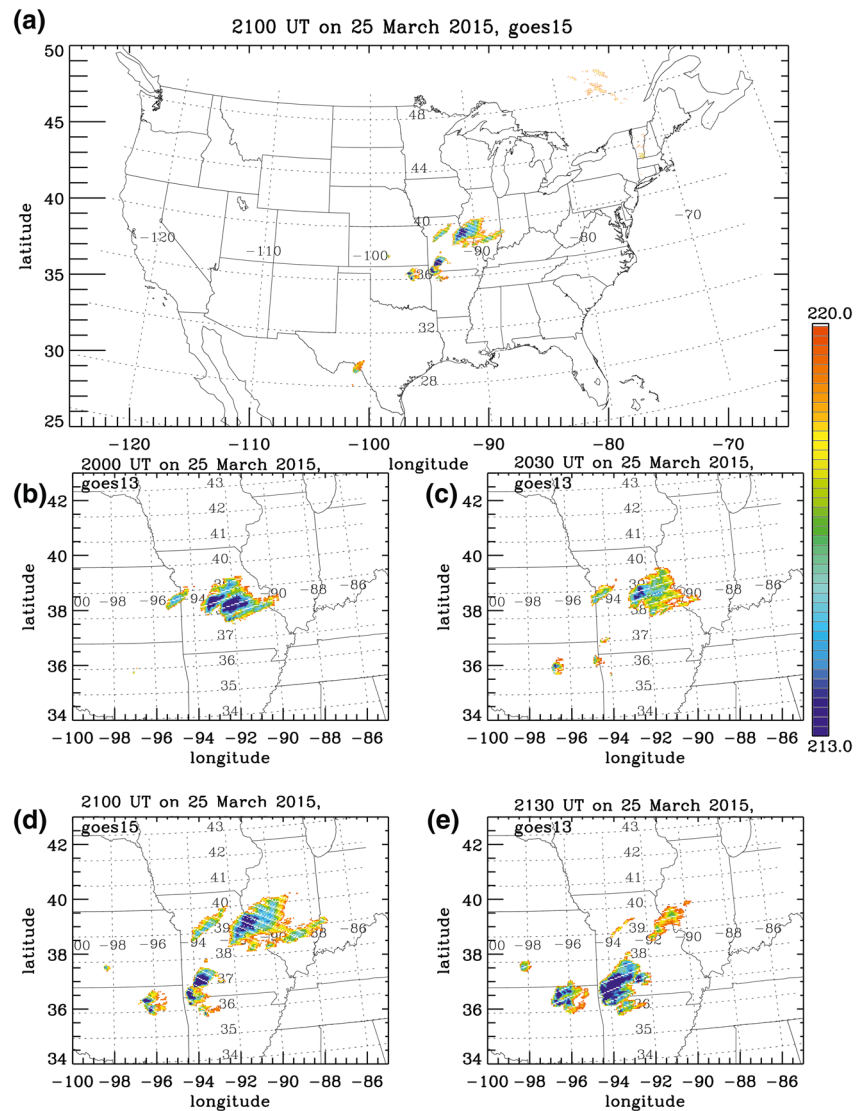


**Figure 12.** Derived cloud top (brightness) temperature (colors), in (K) on March 25 from GOES satellites. (a) 21:00 UT, (b) 20:00 UT, (c) 20:30 UT, (d) 21:00 UT, (e) 21:30 UT.

#### 4.5. Asymmetry of the Concentric Rings and Implication for its Source

For most of the maps shown in Figures 3 and 4, there is marked decrease in the amplitudes of the TIDs propagating northwestward and southeastward at an approximate angle  $\Delta\theta \sim 45^\circ$  from the east-west line at  $36.75^\circ\text{N}$ . These directions are illustrated at 22:40 UT in Figure 6b with green lines. In addition, the amplitudes of the eastward and northeastward GWs are often much larger than the amplitudes of the northwestward and southeastward GWs (see Figures 3b, 3d,, and 6b). This asymmetry in the circular ring pattern could be due to (1) wind/dissipative filtering of an initially symmetric GW field; (2) to an asymmetry of the neutral-ion coupling; or (3) to an initially asymmetric GW field. We now discuss these three possibilities.

First, the neutral wind in the F region is northeastward and eastward at the times of these maps, and would therefore dissipate northeastward GWs much more than southeastward and northwestward propagating GWs (Fritts & Vadas, 2008). This is not observed. Therefore, wind/dissipative filtering cannot explain this asymmetry. Second, although GWs induce TIDs via neutral-ion collisions, the amplitude of a TID depends on  $\mathbf{v} \cdot \mathbf{B}$ , where  $\mathbf{v}$  is the GW velocity vector (Nicolls et al., 2014). Thus, if a symmetric concentric GW field with equal amplitudes at all  $\theta$  propagates within the F region, those GWs propagating geomagnetically

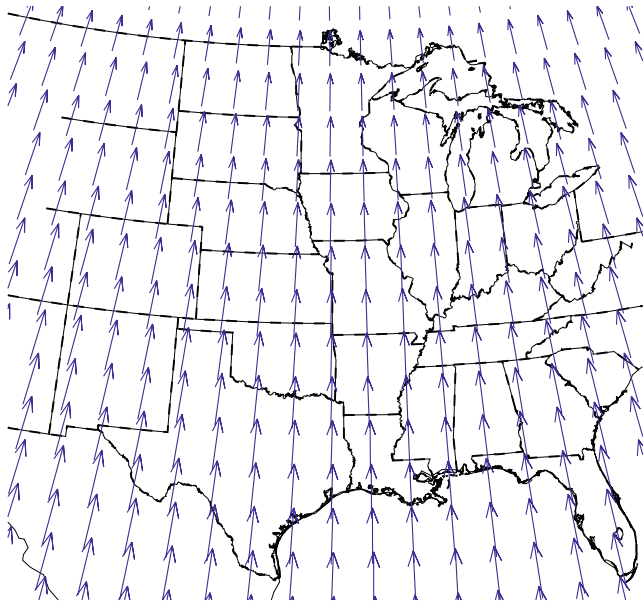


**Figure 13.** Magnetic field  $B$  from the IGRF model at  $z = 300$  km on March 25, 2015 (blue vectors). IGRF, International Geomagnetic Reference Field.

northward and southward will induce TIDs with larger amplitudes than those propagating geomagnetically eastward and westward. Figure 13 shows the Earth's magnetic field lines from the International Geomagnetic Reference Field model. We see that  $B$  is roughly geographically northward over the region of interest. Therefore, neutral-ion coupling cannot explain this asymmetry either.

Third, we reasoned above that the thermospheric source for most of the concentric GWs is likely a horizontal body force created by the dissipation of primary GWs from deep convection. This force creates an asymmetric GW field such that the GWs have maximum amplitudes along and against the force direction, and zero amplitudes perpendicular to the force direction (Vadas et al., 2003, 2018). This agrees well with the asymmetry seen in Figures 3, 4, and 6. Therefore, this asymmetry is most likely due to an initially asymmetric GW field from a local horizontal body force. To create this asymmetry, the body force would need to be directed  $\sim 45^\circ$  northeastward or  $\sim 45^\circ$  southwestward. In the previous section, we found that the center of the TID rings is mainly southwest of the strongest deep convection, thereby implying that southwestward primary GWs from deep convection created southwestward body forces when these GWs dissipated in the thermosphere. Therefore, we suggest that the thermospheric body force which excited most of the largest-amplitude concentric secondary GWs shown in Figure 8 was likely directed southwestward.

## 5. Secondary Gravity Waves on March 26, 2015

### 5.1. GPS TEC Measurements and Comparison With Point Source Theory

Figure 14 shows the GPS TEC maps on March 26, 2015 at 00:55, 01:10, 01:15, and 01:25 UT. Southwestward and westward-propagating partial concentric rings of TIDs are seen sweeping across the southwestern US. Figure 15 shows the TEC perturbations from the estimated ring center of  $36.15^\circ\text{N}$  and  $95.85^\circ\text{W}$  along the angles  $\theta = 195^\circ, 205^\circ, 215^\circ$  and  $220^\circ$  from 01:16 to 01:22 UT. As before, we use a short time interval when the concentric TIDs have the strongest amplitudes and appear clearly in the TEC maps. The dashed, slanted lines show the radial locations of the TID wavefronts having the largest amplitudes as functions of time. Note that there are also smaller-amplitude TIDs in Figure 15 which we do not analyze here. Figure 16 shows  $c_H$  deduced from these dashed lines as a function of  $\mathcal{R}$ . We see that  $c_H$  increases linearly with  $\mathcal{R}$  for these largest-amplitude concentric TIDs, and ranges from  $c_H = 270\text{--}530$  m/s for  $\mathcal{R} \sim 300$  to  $800$  km. These latter horizontal phase speeds are extremely large, and preclude their source being below the turbopause (see Section 4.3). Comparing with Figure 8, the TIDs in Figure 16 have much larger  $c_H$  for similar radii, thereby showing that the underlying GWs here have a different source (with different characteristics) than the GWs shown in Figure 8. Assuming that  $\bar{U}$  and  $\bar{V}$  do not change very much over these values of  $\theta$  and  $\mathcal{R}$  from the location of the point source, we deduce that  $c_{IH}$  also increases approximately linearly with  $\mathcal{R}$ . Thus, we conclude from Equation 13 that all of the GWs which induced the concentric TIDs seen in Figure 16 likely originated from the same point source.

### 5.2. Possible Source Altitudes for the Concentric GWs

We now determine the minimum altitudes that the GWs in Figure 16 can propagate from. Figure 17 shows the background atmosphere at 01:00 UT on March 26. The wind is eastward in the F region, with  $\bar{U} \sim 50\text{--}90$  m/s. The sound speed is a minimum at  $z \simeq 96$  km with  $c_s \sim 270$  m/s. Since  $\bar{U} \sim 10$  m/s at  $z = 96$  km from Figure 17a westward GW needs  $c_H \leq 233$  m/s to propagate through this region. Figures 18a and 18b show  $c_{IH} / \left[ \frac{2\sqrt{\gamma-1}}{\gamma} c_s \right]$  as functions of  $c_H$  and  $z$  for GWs propagating at  $\theta = 195^\circ$  and  $\theta = 220^\circ$ , re-

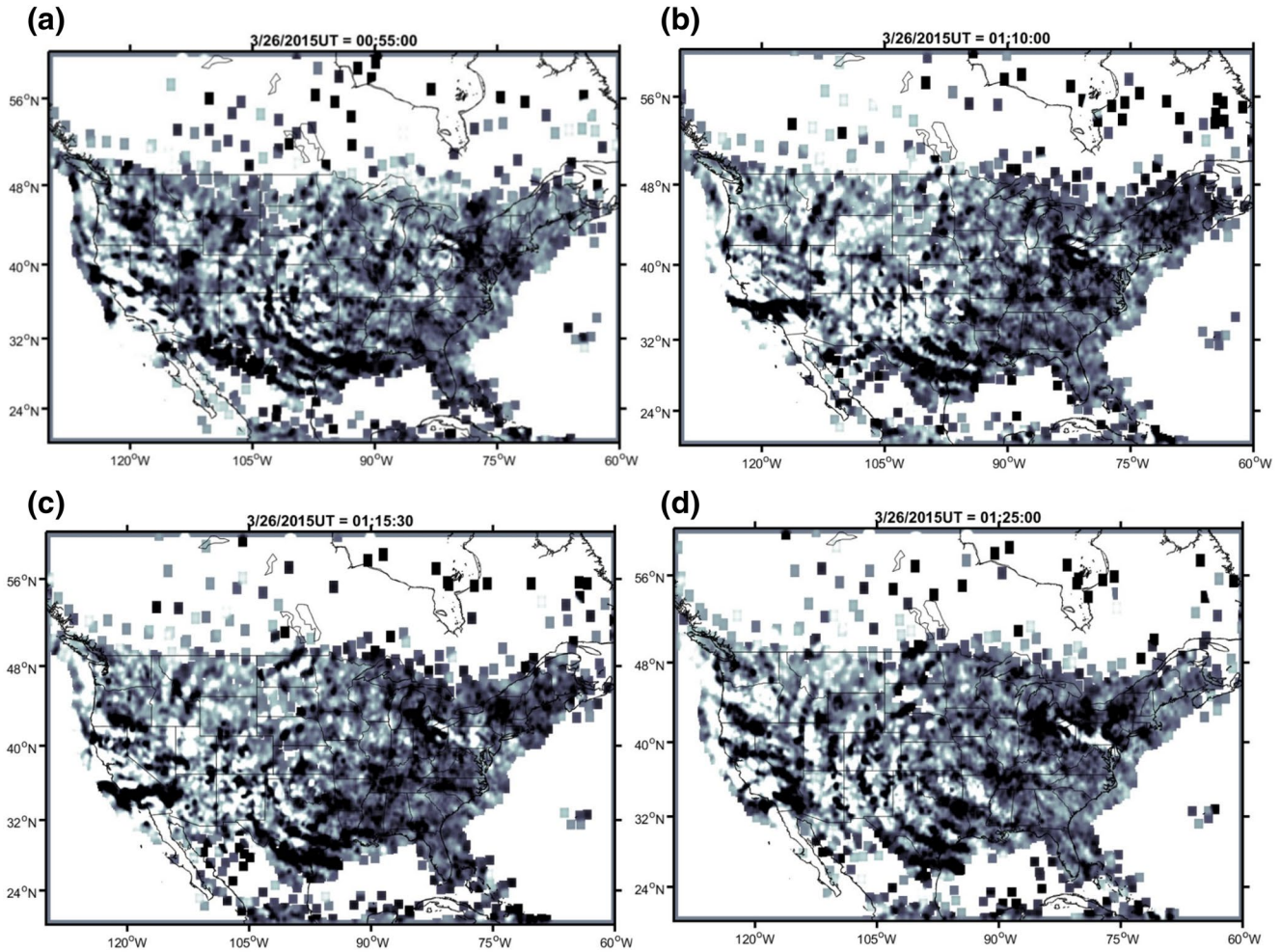


**Figure 14.** GPS TEC maps over the CONUS on March 26, 2015 at (a) 00:55, (b) 01:10, (c) 01:15, and (d) 01:25 UT. CONUS, continental United States.

spectively. Using Equation 17, we see that a GW with  $c_H > 270$  m/s cannot propagate below  $z < 100$  km, and that GWs with  $c_H \sim 220$ – $270$  m/s cannot propagate through  $z \sim 90$ – $110$  km (without tunneling). Combining this with the result from Section 5.1, we find that all of the concentric GWs in Figure 16 were most likely created in the thermosphere, and are therefore likely not primary GWs excited by deep convection.

### 5.3. Spectrograms of the Concentric TIDs

We now calculate the spectrograms of the TIDs on March 26 at 01:34 UT. Figure 19a shows the spectrogram as a function of  $\tau_r$  and longitude at  $36.75^\circ\text{N}$ . For the westward-propagating concentric TIDs, the peak of the spectrogram varies approximately linearly with  $\mathcal{R}$ , with  $\tau_r \sim 10$ – $40$  min. This is consistent with the behavior of GWs excited by a point source. From Figures 11 and 17,  $\bar{U} \sim 80$  m/s near the peak of the F region. Therefore, we estimate  $U_H = -80$  m/s for the westward-propagating TIDs. We also choose  $\Delta z = 190$  km and  $\tau_B = 7$  min (see below). We overplot  $\tau_{Ir}$  for a point source located at  $36.75^\circ\text{N}$  and  $94.85^\circ\text{W}$  using Equation 4 in Figure 19a (white line). We estimate  $\tau_r$  from Equation 18, with  $c_H$  given by the best-fit line in Figure 16. We overplot  $\tau_r$  in Figure 19a as a green line. Here, we choose  $\Delta z = 190$  km and  $\tau_B = 7$  min in order that the green line agrees reasonably well with the peak of the spectrogram. Note that the curves for  $\tau_r$  and  $\tau_{Ir}$  are not best-fit curves, but are intended to show the consistency between the data and point source theory.

Figure 19b shows the spectrogram as a function of  $\lambda_H$  and longitude at  $36.75^\circ\text{N}$ . The peak of the spectrogram increases rapidly with  $\mathcal{R}$  for the westward TIDs, consistent with the quadratic dependence of  $\lambda_H$  on  $\mathcal{R}$  for

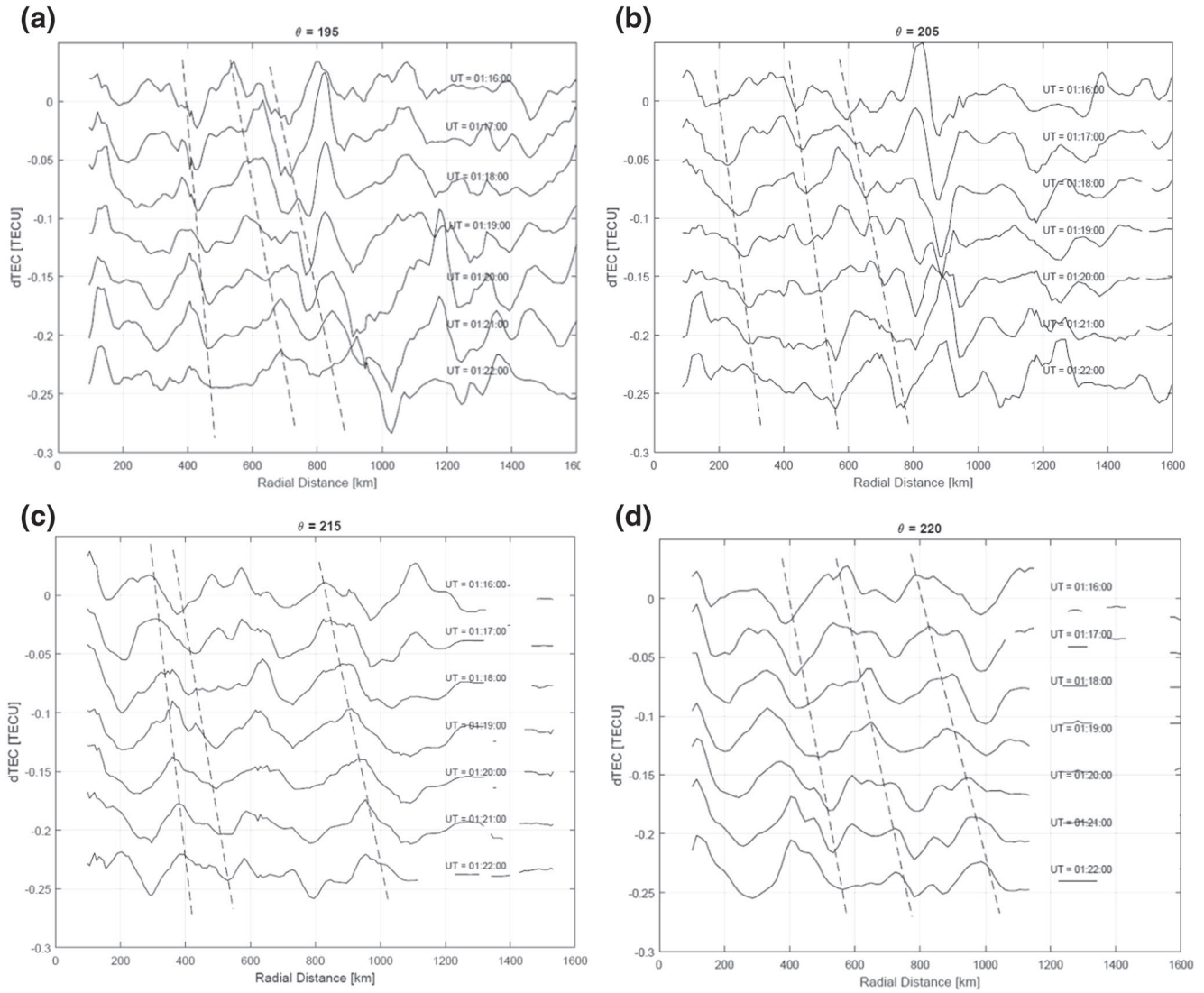


**Figure 15.** The TEC perturbation,  $dTEC$ , (in TECU) as a function of  $\mathcal{R}$  from the estimated ring center at  $36.15^\circ\text{N}$  and  $95.85^\circ\text{W}$  along various angles. The results are shown every minute from 01:16 to 01:22 UT on March 26, 2015, and are offset by 0.04 TECU from top to bottom (solid curves). In addition, solid slant lines are shown which trace out the outward motion of the phase lines of the largest-amplitude concentric TIDs in time. (a)  $\theta = 195^\circ$ . (b)  $\theta = 205^\circ$ . (c)  $\theta = 215^\circ$ . (d)  $\theta = 220^\circ$ . TEC, total electron content; TID, traveling ionospheric disturbance.

GWs excited by a point source (see Equation 8). Typical values for these TIDs are  $\lambda_H \sim 100\text{--}450$  km. We also overplot lines of constant  $c_{gz}$  using Equation 8, with  $\Delta z = 190$  km and  $\tau_B = 7$  min. The curve which shows good consistency between the idealized theory and data is  $c_{gz} = 40$  m/s. From Equation 19, we estimate the time it takes the GWs created by a thermospheric source to propagate to the F region and perturb the TEC to be  $\Delta t \sim 1.3$  h. Using  $z_{bf} \sim 140$  km, we estimate that the GWs perturbed the TEC at  $z \sim z_{bf} + \Delta z \sim 330$  km, which is close to the F-region peak. Using the previous estimate that the primary GWs from deep convection take about 1.0–1.5 h to create a thermospheric body force, we estimate that the deep convective plumes that eventually created the secondary GWs in Figures 14–16 (i.e., at 1.25–1.5 UT) likely occurred at 22.5–23.2 UT on March 25.

Figure 20a shows the cloud top temperatures at 23:00 UT on March 26 over the CONUS. This deep convection is stronger than a few hours earlier, and occurred over Missouri, Nebraska, Oklahoma, and Arkansas. Figures 20b–20d show the cloud top temperatures from 22:00 to 23:30 UT every 30 min. At 22.5–23.2 UT, there are deep convective plumes within a few hundred kilometers from the center of the concentric TID

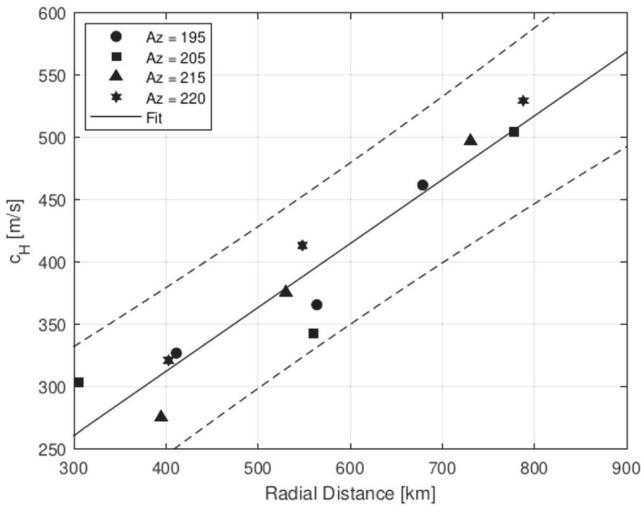


**Figure 16.** The horizontal phase speed,  $c_H$ , of the TIDs as a function of  $\mathcal{R}$  from the estimated ring center at  $36.15^\circ\text{N}$  and  $95.85^\circ\text{W}$ . Here,  $c_H$  is deduced from the dashed lines in Figure 15. Filled circles, squares, triangles and asterisks show the results for  $\theta = 195^\circ, 205^\circ, 215^\circ$ , and  $220^\circ$ , respectively. The black line shows the best fit to these data points. Dashed lines show 95% confidence intervals. TID, traveling ionospheric disturbance.

rings (i.e., at  $36.15^\circ\text{N}$  and  $95.85^\circ\text{W}$ ). Note that the center of these rings is southwest of the strongest deep convection. From Equation 21, this distance is reasonable for the dissipation of southwestward primary GWs from deep convection. This implies that the most likely source of the concentric secondary GWs in Figure 16 are southwestward thermospheric body forces created by the dissipation of southwestward-propagating primary GWs from deep convection.

## 6. Source Estimation via Reverse Ray Tracing

We now ray trace the GWs observed on March 25–26. The ray trace model we use here includes temporally and spatially varying background wind and temperature, kinematic viscosity, and thermal diffusivity in the thermosphere (Vadas & Fritts, 2005), and a varying molecular viscosity  $\mu$  with height above  $z > 220$  km (Vadas & Crowley, 2017; Vadas et al., 2019). We choose a Prandtl number of  $Pr = 0.62$ . We select 11 GWs launched at 23.33 UT on March 25 and 11 GWs launched at 1.567 UT on March 26. Each set of 11 GWs are equally spaced from  $\mathcal{R} = 440$  km (on March 25) and  $\mathcal{R} = 300$  km (on March 26) to  $\mathcal{R} = 800$  km, in accordance with the data shown in Figures 8 and 16, respectively. For each radius, we determine  $c_H$  from the best-fit lines from Figures 8 and 16 on March 25 and 26, respectively. We estimate  $\lambda_H$  from the solid white curves in Figures 10b and 19b. We estimate the observed period from Equation 10:  $\tau_r = \lambda_H/c_H$ .

For consistency with the GW dispersion relation used in the ray trace model,  $\lambda_H$ ,  $\lambda_z$ , and  $\tau_r$  are then iterated so they satisfy the anelastic dissipative GW dispersion relation while keeping  $c_H$  constant. The propagation angles are chosen randomly from  $\theta = 180$ – $220^\circ$  with respect to the estimated ring centers of  $36.75^\circ\text{N}$  and  $94.85^\circ\text{W}$  for March 25 and  $36.15^\circ\text{N}$  and  $95.85^\circ\text{W}$  for March 26. The GWs are launched at  $z = 300$  km.

Figure 21a shows the reverse ray trace results as functions of  $z$  and time for the case on March 25. Each GW's source can be located anywhere along its reverse ray trace "line." The colored dot shows the minimum possible altitude for each GW, which ranges from 0 to 115 km. We see that 8 out of the 11 (or 73%) of the GWs could not have been created below  $z = 100$  km. Since all of the GWs most likely originated from the same source (see Figure 8), we conclude that all of the GWs in Figure 21a most likely originated above  $z > 100$  km.

Figure 21a also shows the forward ray trace results. A square shows where each GW's vertical flux of horizontal momentum (per unit mass),  $\overline{u'_H w'}$ , is maximum (called " $z_{\text{diss}}$ "). Above this altitude,  $\overline{u'_H w'}$  decreases rapidly because of viscosity (Vadas, 2007). Most of the GWs have their maximum amplitudes near  $z = 300$  km.

Figures 21b and 21c show the same results as in Figure 21a, except as a function of  $c_H$  versus  $z$  and  $c_{\text{TH}}$  versus  $z$ , respectively. It is clear that none of the GWs with  $c_H > 200$  m/s can propagate from below the turbopause into the thermosphere.

Figure 21d shows the reverse ray trace results on a U.S. map. The starting location for each GW is denoted by an asterisk. Each GW's source is located anywhere along its colored line. The colored dots correspond to the same times/locations as the colored dots in Figures 21a–21c, which indicates the location where each GW could have had its minimum altitude. Most of the lines converge near the intersection of Missouri, Nebraska, Oklahoma, and Arkansas, at the location  $95.85^\circ\text{W}$  and  $36.9^\circ\text{N}$  (triangle). This is close to the inferred TID ring center (diamond). From Figure 12 the strongest deep convection occurs at  $92$ – $95^\circ\text{W}$  and  $36$ – $39^\circ\text{N}$  on March 25. Therefore, the approximate location of the thermospheric source at  $\sim 95.85^\circ\text{W}$  and  $\sim 36.9^\circ\text{N}$  is several hundred kilometers, or  $\sim 2$ – $4^\circ$  from the strongest deep convection. This is consistent with the close proximity of thermospheric body forces to deep convection (see Equations 20 and 21).

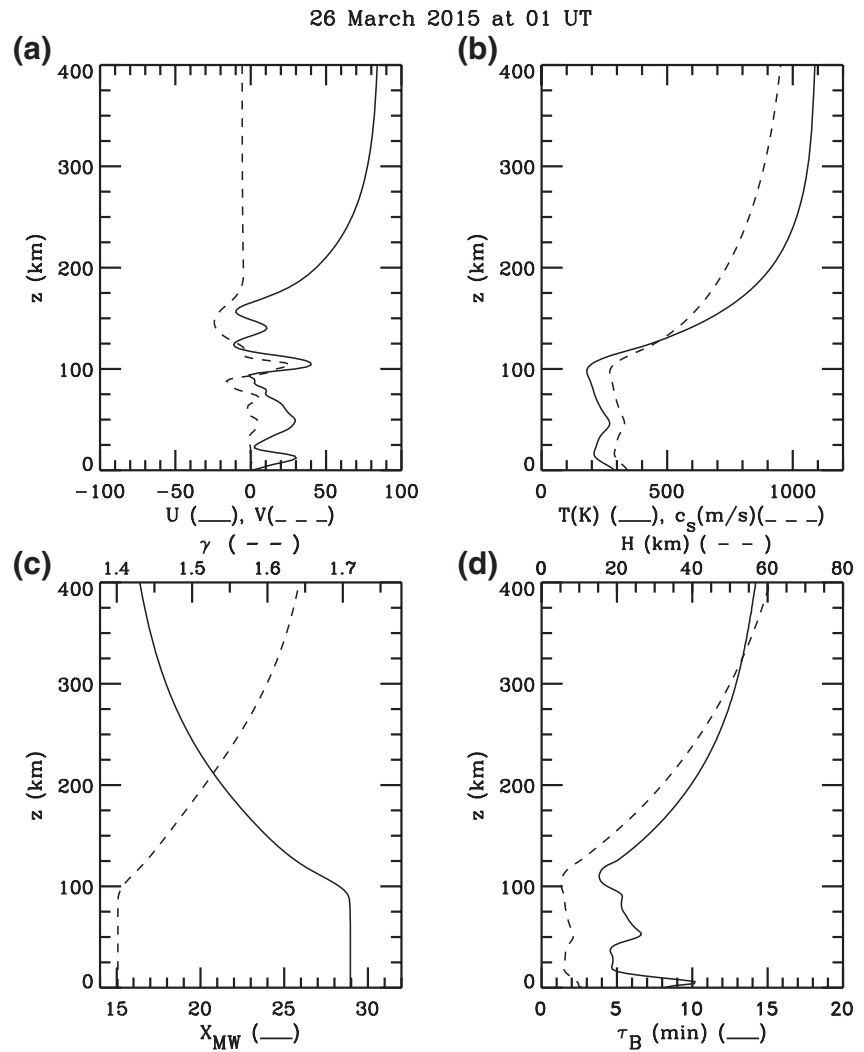


Figure 17. Same as in Figure 5 but for 01:00 UT on March 26.

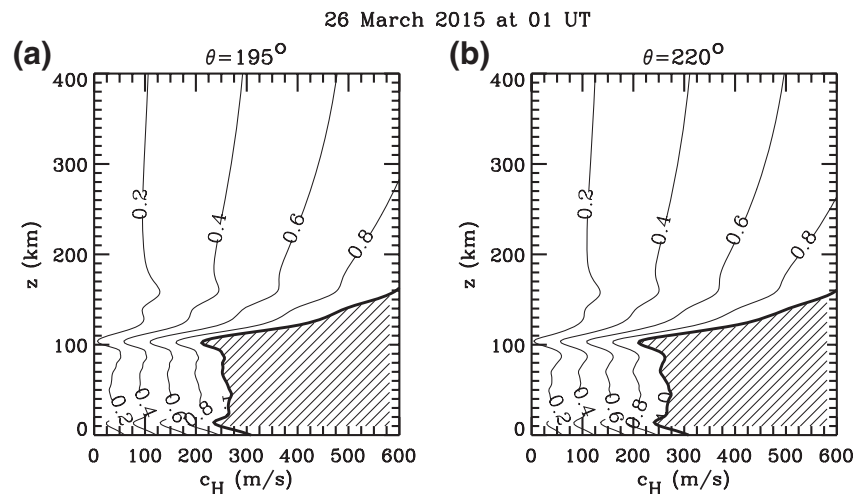
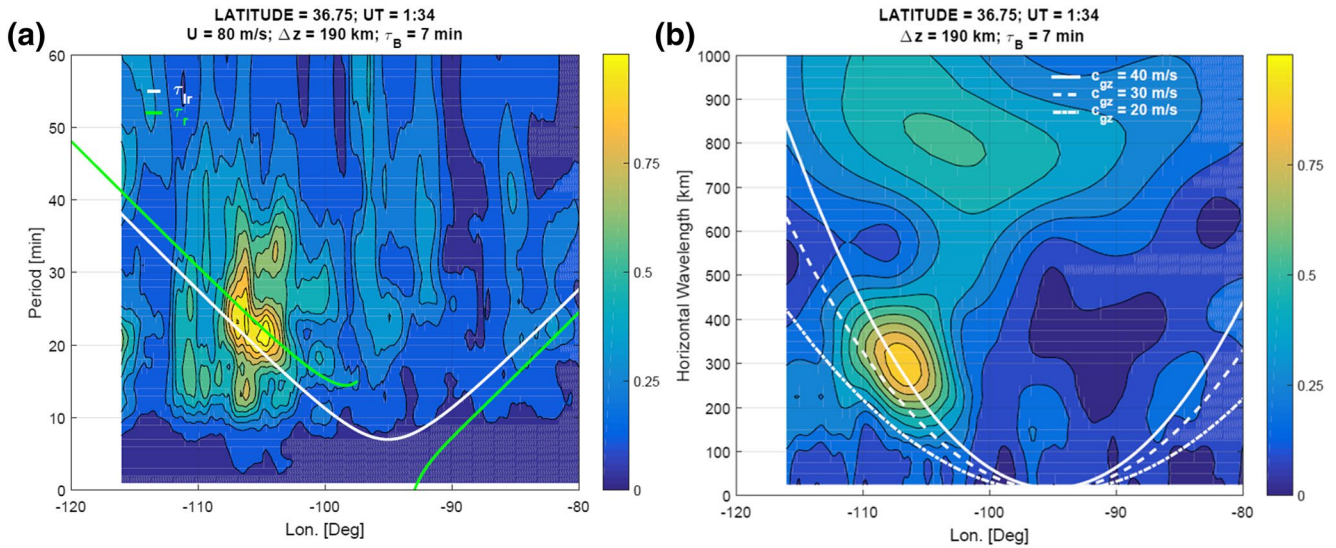


Figure 18. Same as in Figure 9 but for 01:00 UT on March 26 and for (a)  $\theta = 195^\circ$  and (b)  $\theta = 220^\circ$ .



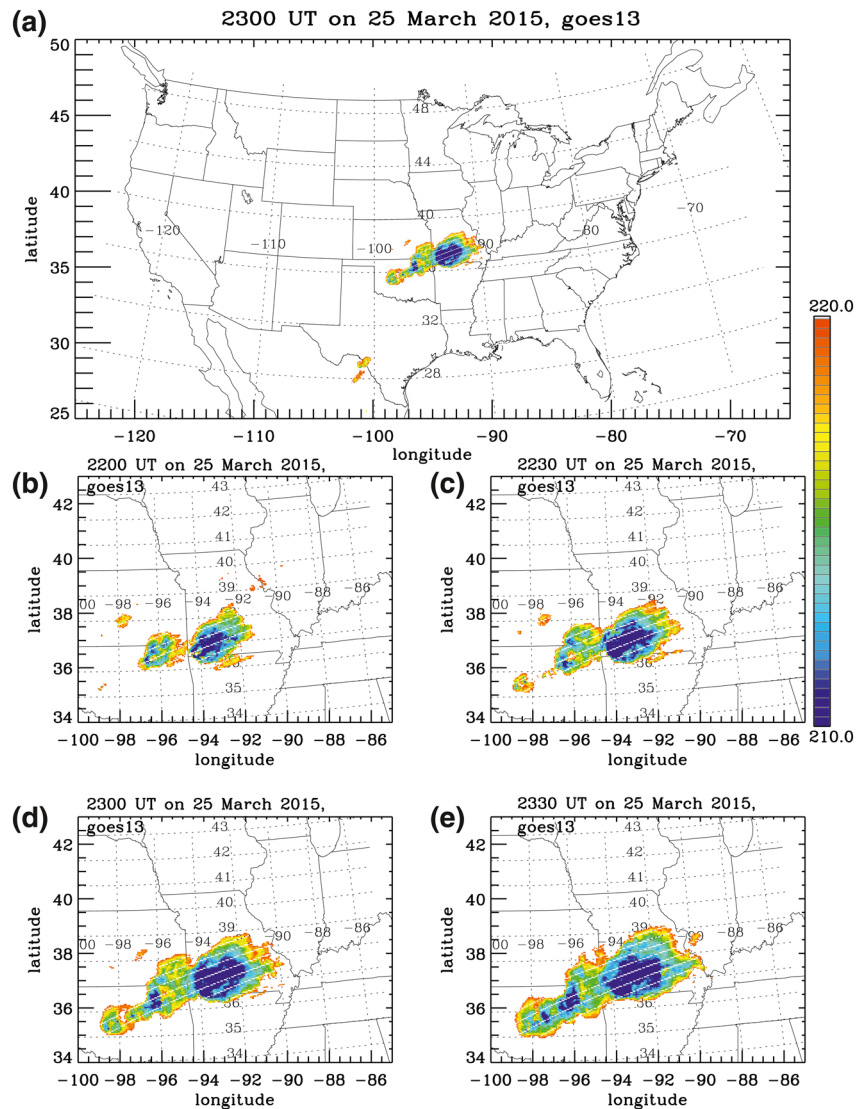
**Figure 19.** Spectrograms of the TIDs at 01:34 UT on March 26 at 36.75°N. (a) Spectrogram as a function of period and longitude (colors). The green and white lines show the observed and intrinsic periods, respectively, for GWs excited by a point source assuming  $\bar{U} = 80$  m/s,  $\Delta z = 190$  km, and  $\tau_B = 7$  min (see text). (b) Spectrogram as a function of the horizontal wavelength and longitude (colors). The dot, dash and solid white lines show  $c_{gz} = 20, 30$ , and  $40$  m/s, respectively, for GWs excited by a point source in an idealized atmosphere using Equation 8 and assuming  $\Delta z = 190$  km and  $\tau_B = 7$  min (see text). GW, gravity wave; TID, traveling ionospheric disturbance.

Figure 22 shows the ray trace results for the case on March 26. The minimum possible altitudes range from 110 to 140 km. Therefore, none of the GWs could have been created below  $z = 110$  km; we conclude that all of the GWs for this case originated in the thermosphere. In Figure 22d, most of the lines converge near the intersection of Nebraska and Oklahoma, at the location 96.75°W and 36.75°N (triangle). This is close to the inferred TID ring center (diamond). From Figure 20 the strongest deep convection occurs at 92–95°W and 36–38°N on March 26. Therefore, the approximate location of the thermospheric source at 96.75°W and 36.75°N is  $\sim 2$ – $4^\circ$  from the strongest deep convection, consistent with the close proximity of thermospheric body forces to deep convection.

## 7. Conclusions

In this study, we examined two cases separated by a few hours in the GPS TEC data over the CONUS at approximately  $\sim 23:00$  UT on March 25 and at  $\sim 01:20$  UT on March 26, 2015. For these cases, (1) partial to nearly fully concentric rings that spanned up to  $\sim 330^\circ$  in azimuth were seen; (2) the apparent centers of the rings were close to regions of strong deep convection; and (3) some of the concentric TIDs had observed horizontal phase speeds of  $c_H > 300$  m/s. Because of the fast horizontal phase speeds, we investigated if some of these concentric TIDs could be induced by secondary GWs from deep convection. For these cases, we found that  $c_H$  increased linearly with radius  $\mathcal{R}$  from the inferred center of the rings, with  $c_H = 150$ – $370$  m/s and  $c_H = 270$ – $530$  m/s on March 25 and 26, respectively. We also found that the inferred GW period,  $\tau_r$ , increased roughly linearly with  $\mathcal{R}$ , with  $\tau_r \sim 8$ – $40$  min. Finally, we found that the horizontal wavelength,  $\lambda_H$ , increased approximately quadratically with  $\mathcal{R}$ , with  $\lambda_H \sim 100$ – $500$  km. These results are consistent with the GWs for each case being created by a single point source.

Using reverse ray tracing, we found that those concentric GWs with  $c_H > 200$  m/s could not have propagated below  $z = 100$  km, because the sound speed is too small below the turbopause. This is because the maximum intrinsic horizontal phase speed a GW can have is  $90\%$   $c_s$  below the turbopause. We found that for the case on March 25,  $\sim 73\%$  of the underlying GWs could not have propagated below  $z \sim 100$  km and therefore must have been created at  $z > 100$  km. For the case on March 26, none of the underlying GWs could have propagated below  $z < 110$  km and therefore must have been created in the thermosphere. We also found that the reverse ray-traced GWs converged (backwards in time) to a point  $\sim 2$ – $4^\circ$  from the centers of the



**Figure 20.** Derived cloud top (brightness) temperature (colors, in (K) on March 25 from GOES satellites. (a) 23:00 UT, (b) 22:00 UT, (c) 22:30 UT, (d) 23:00 UT, (e) 23:30 UT.

strongest deep convection for both cases. Combining these results, we conclude that for each case, all of the concentric GWs (even those with  $c_H \approx 150\text{--}200$  m/s) were most likely created from the same “point” source in the thermosphere, and that these sources were most likely local horizontal body forces created from the dissipation of high-frequency primary GWs from deep convection. Therefore, we conclude that the concentric GWs that induced the concentric TIDs were most likely secondary GWs from deep convection. In order to prove definitively that the GWs with  $c_H \approx 150\text{--}200$  m/s ( $\sim 14\%$  of the GWs studied here) were created in the thermosphere, detailed forward modeling studies would need to be performed. Such studies are out of the scope of the present paper.

Because of the close proximity of the centers of the concentric GW rings with strong deep convection ( $\sim 2\text{--}4^\circ$ ), one could easily mistakenly assume that these concentric GWs are primary GWs excited by deep convection (which is also possible). This is why it is important to carefully analyze the TID wavefronts, as was done in Figures 7, 8, 15, and 16.

Finally, our result implies that the horizontal phase speeds for the spectra of primary and secondary GWs from deep convection most likely overlap for  $c_H \sim 100\text{--}200$  m/s. This overlap was noted previously by Vadas

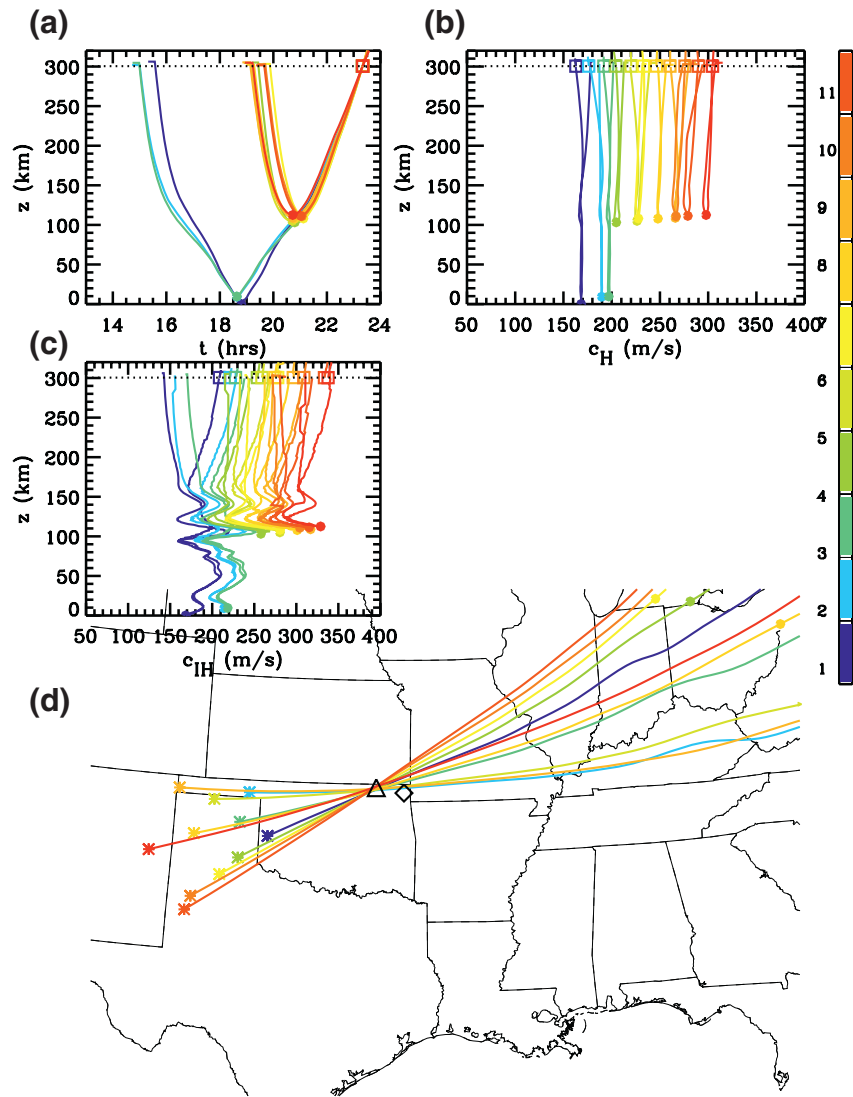


**Figure 21.** Ray trace results for 11 GWs launched at 23.33 UT on March 25 at  $z = 300$  km. The color shows the GW #. (a)  $z$  versus time. The source of each GW is located anywhere along its colored line before launch. The colored dots indicate the minimum possible altitudes that each GW can propagate. The dotted line shows  $z = 300$  km, and the colored squares show  $z_{\text{diss}}$ . (b and c) Same as in (a), but for  $c_H$  versus  $z$  and  $c_{IH}$  versus  $z$ , respectively. (d) Reverse ray trace results for each GW. The asterisks show the launch locations at  $z = 300$  km. The source of each GW is located anywhere along its colored line. The colored dots show the locations of the minimum possible altitudes (identical to the colored dots in a–c). The triangle is at  $95.85^\circ\text{W}$  and  $36.9^\circ\text{N}$ . The diamond shows the center of the concentric TIDs. GW, gravity wave; TID, traveling ionospheric disturbance.

and Crowley (2010), who found that the secondary GWs from deep convection had  $c_H \sim 100\text{--}600$  m/s. A future study will (forward) model the primary and secondary GWs from deep convection that occurred during this and/or other events, and will compare the results with TEC observations.

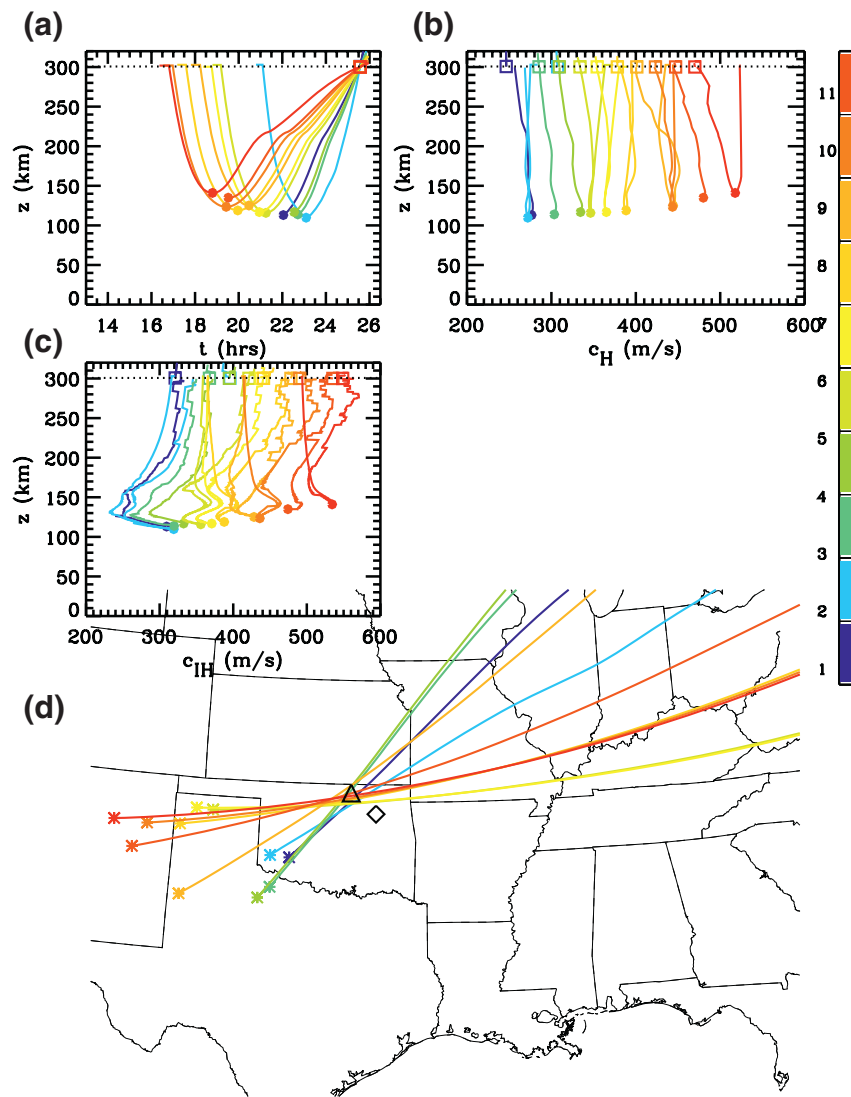


**Figure 22.** Same as in Figure 21, except for the 11 GW launched at 1.567 UT on March 26. The triangle is at 96.75°W and 36.75°N. GW, gravity wave.

### Data Availability Statement

GOES data is available at [http://www.class.noaa.gov/saa/products/search?datatype\\_family=GVAR\\_IMG](http://www.class.noaa.gov/saa/products/search?datatype_family=GVAR_IMG). We acknowledge the use of publicly available ground-based GPS TEC data from the Southern California Integrated GPS Network, International GPS Service for Geodynamics, UNAVCO, Hartebeesthoek Radio Astronomy Observatory, National Oceanic and Atmospheric Administration, and National Aeronautics and Space Administration. The model data shown in this study are available via NWRA's website at <https://www.cora.nwra.com/vadas/Vadas-et-al-JGR-2020-March2015-files/>.

### Acknowledgments

We would like to thank Katrina Bossert for help converting GOES data to brightness temperatures. Sharon L. Vadas was supported by NSF Grant AGS-1552315 and by NASA grants 80NSSC19K0836 and 80NSSC20K0628. Irfan Azeem was supported by NSF grant AGS-1552310 to ASTRA.

### References

- Alexander, M. J., Holton, J. R., & Durran, D. R. (1995). The gravity wave response above deep convection in a squall line simulation. *Journal of Atmospheric Science*, 52(12), 2212–2226. <https://doi.org/10.1175/1520-0469>
- Azeem, I., & Barlage, M. (2017). Atmosphere-ionosphere coupling from convectively generated gravity waves. *Advances in Space Research*, 61, 1931–1941. <https://doi.org/10.1016/j.asr.2017.09.029>
- Azeem, I., Vadas, S. L., Crowley, G., & Makela, J. (2017). Traveling ionospheric disturbances over the United States induced by gravity waves from the 2011 Tohoku tsunami and comparison with gravity wave dissipative theory. *Journal of Geophysical Research: Space Physics*, 122, 3430–3447. <https://doi.org/10.1002/2016JA023659>

- Azeem, I., Yue, J., Hoffmann, L., Miller, S. D., Starka, W. C., III, & Crowley, G. (2015). Multisensor profiling of a concentric gravity wave event propagating from the troposphere to the ionosphere. *Geophysical Research Letters*, *42*, 7874–7880. <https://doi.org/10.1002/2015GL065903>
- Choi, H.-J., Chun, H.-Y., & Song, I.-S. (2007). Characteristics and momentum flux spectrum of convectively forced internal gravity waves in ensemble numerical simulations. *Journal of the Atmospheric Sciences*, *64*(10), 3723–3734.
- Chou, M. Y., Lin, C. C. H., Yue, J., Tsai, H. F., Sun, Y. Y., Liu, J. Y., & Chen, C. H. (2017). Concentric traveling ionosphere disturbances triggered by Super Typhoon Meranti (2016). *Geophysical Research Letters*, *44*, 1219–1226. <https://doi.org/10.1002/2016GL072205>
- Chun, H.-Y., & Kim, Y.-H. (2008). Secondary waves generated by breaking of convective gravity waves in the mesosphere and their influence in the wave momentum flux. *Journal of Geophysical Research*, *113*, D23. <https://doi.org/10.1029/2008JD009792>
- Crowley, G., Azeem, I., Reynolds, A., Duly, T. M., McBride, P., Winkler, C., & Hunton, D. (2016). Analysis of traveling ionospheric disturbances (TIDs) in GPS TEC launched by the 2011 Tohoku earthquake. *Radio Science*, *51*, 507–514. <https://doi.org/10.1002/2015RS005907>
- Djuth, F. T., Sulzer, M. P., Elder, J. H., & Wickwar, V. B. (1997). High-resolution studies of atmosphere-ionosphere coupling at Arecibo Observatory, Puerto Rico. *Radio Science*, *32*, 2321–2344. <https://doi.org/10.1029/97RS02797>
- Djuth, F. T., Sulzer, M. P., Gonzáles, S. A., Mathews, J. D., Elder, J. H., & Walterscheid, R. L. (2004). A continuum of gravity waves in the Arecibo thermosphere?. *Geophysical Research Letters*, *31*, L16801. <https://doi.org/10.1029/2003GL019376>
- Drob, D. P., Emmert, J. T., Meriwether, J. W., Makela, J. J., Doornbos, E., Conde, M., et al. (2015). An update to the Horizontal Wind Model (HWM): The quiet time thermosphere. *Earth and Space Science*, *2*, 301–319. <https://doi.org/10.1002/2014EA000089>
- Fritts, D. C., & Vadas, S. L. (2008). Gravity wave penetration into the thermosphere: sensitivity to solar cycle variations and mean winds. *Annals of Geophysics*, *26*, 3841–3861. <https://doi.org/10.5194/angeo-26-3841-2008>
- Heale, C. J., Snively, J. B., Hickey, M. P., & Ali, C. J. (2014). Thermospheric dissipation of upward propagating gravity wave packets. *Journal of Geophysical Research*, *119*, 3857–3872. <https://doi.org/10.1002/2013JA019387>
- Hedin, A. (1991). Extension of the MSIS thermosphere model into the middle and lower atmosphere. *Journal of Geophysical Research*, *96*, 1159.
- Hickey, M. P., Schubert, G., & Walterscheid, R. L. (2009). The propagation of tsunami-driven gravity waves into the thermosphere and ionosphere. *Journal of Geophysical Research*, *114*(A08), 304. <https://doi.org/10.1029/2009JA014105>
- Hocke, K., & Schlegel, K. (1996). A review of atmospheric gravity waves and traveling ionospheric disturbances: 1982–1995. *Annals of Geophysics*, *14*, 917–940
- Holton, J., & Alexander, M. (1999). Gravity waves in the mesosphere generated by tropospheric convection. *Tellus*, *51A-B*, 45–58.
- Kaplan, E. D., & Hagerty, C. (2006). *Understanding GPS: Principles and applications* (2nd ed.). Artech House.
- Lane, T. P., Sharman, R. D., Clark, T. L., & Hsu, H.-M. (2003). An investigation of turbulence generation mechanisms above deep convection. *Journal of the Atmospheric Sciences*, *60*, 1297–1321. <https://doi.org/10.1175/1520-0469>
- Martinis, C., Baumgardner, J., Wroten, J., & Mendillo, M. (2010). Seasonal dependence of MSTIDs obtained from 630.0 nm airglow imaging at Arecibo. *Geophysical Research Letters*, *37*, L11. <https://doi.org/10.1029/2010GL043569>
- Miyoshi, Y., & Fujiwara, H. (2008). Gravity waves in the thermosphere simulated by a general circulation model. *Journal of Geophysical Research*, *113*, D011101. <https://doi.org/10.1029/2007JD008874>
- Nicolls, M. J., Vadas, S. L., Aponte, N., & Sulzer, M. P. (2014). Horizontal wave parameters of daytime thermospheric gravity waves and E-region neutral winds over Puerto Rico. *Journal of Geophysical Research*, *119*, 576–600. <https://doi.org/10.1002/2013JA018988>
- Nicolls, M. J., Varney, R. H., Vadas, S. L., Stamus, P. A., Heinselman, C. J., Cosgrove, R. B., et al. (2010). Influence of an inertia-gravity wave on mesospheric dynamics: A case study with the Poker Flat Incoherent Scatter Radar. *Journal of Geophysical Research*, *115*, D00N02. <https://doi.org/10.1029/2010JD014042>
- Nishioka, M., Tsugawa, T., Kubota, M., & Ishii, M. (2013). Concentric waves and short-period oscillations observed in the ionosphere after the 2013 Moore EF5 tornado. *Geophysical Research Letters*, *40*, 5581–5586. <https://doi.org/10.1002/2013GL057963>
- Oliver, W. L., Otsuka, Y., Sato, M., Takami, T., & Fukao, S. (1997). A climatology of F region gravity wave propagation over the middle and upper atmosphere radar. *Journal of Geophysical Research*, *102*, 14499–14512. <https://doi.org/10.1029/97JA00491>
- Perkins, F. W. (1973). Spread F and ionospheric currents. *Journal of Geophysical Research*, *78*, 218–226.
- Perona, P., & Malik, J. (1990). Scale-space and edge detection using anisotropic diffusion. *IEEE Transactions on Pattern Analysis and Machine Intelligence*, *12*(7), 629–639. <https://doi.org/10.1109/34.56205>
- Piteway, M., & Hines, C. (1963). The viscous damping of atmospheric gravity waves. *Canadian Journal of Physics*, *41*, 1935–1948.
- Roble, R., & Ridley, E. (1994). A thermosphere-ionosphere-mesosphere-electrodynamics general circulation model (TIME-GCM): Equinox solar cycle minimum simulations (30–500 km). *Geophysical Research Letters*, *21*, 417–420.
- Tsugawa, T., Otsuka, Y., Coster, A. J., & Saito, A. (2007). Medium-scale traveling ionospheric disturbances detected with dense and wide TEC maps over North America. *Geophysical Research Letters*, *34*, L22101. <https://doi.org/10.1029/2007GL031663>
- Vadas, S. L. (2007). Horizontal and vertical propagation and dissipation of gravity waves in the thermosphere from lower atmospheric and thermospheric sources. *Journal of Geophysical Research*, *112*, A06305. <https://doi.org/10.1029/2006JA011845>
- Vadas, S. L. (2013). Compressible  $f$ -plane solutions to body forces, heatings, and coolings, and application to the primary and secondary gravity waves generated by a deep convective plume. *Journal of Geophysical Research: Space Physics*, *118*, 2377–2397. <https://doi.org/10.1002/jgra.50163>
- Vadas, S. L., & Becker, E. (2018). Numerical modeling of the excitation, propagation, and dissipation of primary and secondary gravity waves during wintertime at McMurdo Station in the Antarctic. *Journal of Geophysical Research: Atmospheres*, *123*, 9326–9369. <https://doi.org/10.1029/2017JD027974>
- Vadas, S. L., & Becker, E. (2019). Numerical modeling of the generation of tertiary gravity waves in the mesosphere and thermosphere during strong mountain wave events over the Southern Andes. *Journal of Geophysical Research: Space Physics*, *124*, 7687–7718. <https://doi.org/10.1029/2019JA026694>
- Vadas, S. L., & Crowley, G. (2010). Sources of the traveling ionospheric disturbances observed by the ionospheric TIDBIT sounder near Wallops Island on October 30, 2007. *Journal of Geophysical Research: Space Physics*, *115*, A07324. <https://doi.org/10.1029/2009JA015053>
- Vadas, S. L., & Crowley, G. (2017). Neutral wind and density perturbations in the thermosphere created by gravity waves observed by the TIDBIT sounder. *Journal of Geophysical Research: Space Physics*, *122*, 6652–6678. <https://doi.org/10.1002/2016JA023828>
- Vadas, S. L., & Fritts, D. C. (2004). Thermospheric responses to gravity waves arising from mesoscale convective complexes. *Journal of Atmospheric and Solar-Terrestrial Physics*, *66*, 781–804.
- Vadas, S. L., & Fritts, D. C. (2005). Thermospheric responses to gravity waves: Influences of increasing viscosity and thermal diffusivity. *Journal of Geophysical Research*, *110*, D15103. <https://doi.org/10.1029/2004JD005574>
- Vadas, S. L., & Fritts, D. C. (2006). Influence of solar variability on gravity wave structure and dissipation in the thermosphere from tropospheric convection. *Journal of Geophysical Research*, *111*, A10S12. <https://doi.org/10.1029/2005JA011510>

- Vadas, S. L., & Fritts, D. C. (2009). Reconstruction of the gravity wave field from convective plumes via ray tracing. *Annals of Geophysics*, *27*, 147–177.
- Vadas, S. L., Fritts, D. C., & Alexander, M. J. (2003). Mechanisms for the generation of secondary waves in wave breaking regions. *Journal of the Atmospheric Sciences*, *60*, 194–214. <https://doi.org/10.1029/2004JD005574>
- Vadas, S. L., & Liu, H.-L. (2009). Generation of large-scale gravity waves and neutral winds in the thermosphere from the dissipation of convectively generated gravity waves. *Journal of Geophysical Research*, *114*, A10310. <https://doi.org/10.1029/2009JA014108>
- Vadas, S. L., & Liu, H.-L. (2013). Numerical modeling of the large-scale neutral and plasma responses to the body forces created by the dissipation of gravity waves from 6 h of deep convection in Brazil. *Journal of Geophysical Research*, *118*, 2593–2617. <https://doi.org/10.1002/jgra.50249>
- Vadas, S., Liu, H.-L., & Lieberman, R. (2014). Numerical modeling of the global changes to the thermosphere and ionosphere from the dissipation of gravity waves from deep convection. *Journal of Geophysical Research*, *119*, 7762–7793. <https://doi.org/10.1002/2014JA020280>
- Vadas, S. L., & Nicolls, M. J. (2009). Temporal evolution of neutral, thermospheric winds and plasma response using PFISR measurements of gravity waves. *Journal of Atmospheric and Solar-Terrestrial Physics*, *71*, 740–770. <https://doi.org/10.1016/j.jastp.2009.01.011>
- Vadas, S. L., Xu, S., Yue, J., Bossert, K., Becker, E., & Baumgarten, G. (2019). Characteristics of the quiet-time hotspot gravity waves observed by GOCE over the Southern Andes on 5 July 2010. *Journal of Geophysical Research: Space Physics*, *124*, 7034–7061. <https://doi.org/10.1029/2019JA026693>
- Vadas, S., Yue, J., & Nakamura, T. (2012). Mesospheric concentric gravity waves generated by multiple convection storms over the North America Great Plain. *Journal of Geophysical Research*, *117*, D7. <https://doi.org/10.1029/2011JD017025>
- Vadas, S. L., Yue, J., She, C.-Y., Stamus, P., & Liu, A. (2009). A model study of the effects of winds on concentric rings of gravity waves from a convective plume near Fort Collins on 11 May 2004. *Journal of Geophysical Research*, *114*, D06. <https://doi.org/10.1029/2008JD010753>
- Vadas, S. L., Zhao, J., Chu, X., & Becker, E. (2018). The excitation of secondary gravity waves from local body forces: Theory and observation. *Journal of Geophysical Research: Atmospheres*, *123*, 9296–9325. <https://doi.org/10.1029/2017JD027970>
- Xu, S., Yue, J., Xue, X., Vadas, S., Miller, S. D., Azeem, I., et al. (2019). Dynamical coupling between Hurricane Matthew and the middle to upper atmosphere via gravity waves. *Journal of Geophysical Research: Space Physics*, *124*, 3589–3608. <https://doi.org/10.1029/2018JA026453>
- Yiğit, E., Medvedev, A. S., Aylward, A. D., Hartogh, P., & Harris, M. J. (2009). Modeling the effects of gravity wave momentum deposition on the general circulation above the turbopause. *Journal of Geophysical Research*, *114*, D07101. <https://doi.org/10.1029/2008JD011132>
- Yue, J., Vadas, S. L., She, C.-Y., Nakamura, T., Reising, S. C., Liu, H.-L., et al. (2009). Concentric gravity waves in the mesosphere generated by deep convective plumes in the lower atmosphere near Fort Collins. *Journal of Geophysical Research*, *114*, D06104. <https://doi.org/10.1029/2008JD011244>
- Zhou, Q., & Mathews, J. D. (2006). On the physical explanation of the Perkins instability. *Journal of Geophysical Research*, *111*, A12309. <https://doi.org/10.1029/2006JA011696>